Cosmochemical and spectroscopic properties of Northwest Africa 7325 - A consortium study

The Meteoritical Society

Meteoritics & Planetary Science 51, Nr 1, 3–30 (2016)
doi: 10.1111/maps.12586

Cosmochemical and spectroscopic properties of Northwest Africa 7325—A consortium study

I. WEBER[1*], A. MORLOK[1], A. BISCHOFF[1], H. HIESINGER[1], D. WARD[1], K. H. JOY[2], S. A. CROWTHER[2], N. D. JASTRZEBSKI[2], J. D. GILMOUR[2], P. L. CLAY[2], R. A. WOGELIUS[2], R. C. GREENWOOD[3], I. A. FRANCHI[3], and C. MÜNKER[4]

[1]Institut für Planetologie, Wilhelm-Klemm-Str. 10, Westfälische Wilhelms-Münster, 48149 Münster, Germany
[2]School of Earth, Atmospheric and Environmental Sciences, The University of Manchester, Oxford Road, Manchester M13 9PL, UK
[3]Planetary and Space Sciences, The Open University, Milton Keynes MK7 6AA, UK
[4]Institut für Geologie und Mineralogie, Universität zu Köln, Zülpicherstr. 49b, 50674 Köln, Germany
[*]Corresponding author. E-mail: sonderm@uni-muenster.de

(Received 12 January 2015; revision accepted 26 October 2015)

Abstract–This work is part of a project to build an infrared database in order to link IR data of planetary materials (and therefore possible Mercury material) with remote sensing observations of Mercury, which will probably be obtained by the MERTIS instrument on the forthcoming BepiColombo mission.The unique achondrite Northwest Africa (NWA) 7325, which has previously been suggested to represent the first sample from Mercury, was investigated by optical and electron microscopy, and infrared and Raman spectroscopy. In addition, the oxygen, strontium, xenon, and argon isotopes were measured and the abundance of selected trace elements determined. The meteorite is a cumulate rock with subchondritic abundances of HFSE and REE and elevated Sr contents, which underwent a second heating and partial remelting process. Oxygen isotope measurements show that NWA 7325 plots in the ureilite field, close to the ALM-A trachyandesitic fragment found in the unique Almahata Sitta meteorite breccia. On the other hand, mineralogical investigations of the pyroxenes in NWA 7325 provide evidence for similarities to the lodranites and acapulcoites. Furthermore, the rock is weakly shocked and argon isotope data record ancient (~4.5 Ga) plateau ages that have not been reset. The sample records a cosmogenic exposure age of ~19 Ma. Systematics of Rb-Sr indicate an extreme early volatile depletion of the precursor material, similar to many other achondrite groups. However, despite its compositional similarities to other meteorite groups, our results suggest that this meteorite is unique and unrelated to any other known achondrite group. An origin for NWA 7325 as a sample from the planet Mercury is not supported by the results of our investigation. In particular, the evidence from infrared spectroscopy indicates that a direct relationship between NWA 7325 and the planet Mercury can be ruled out: no acceptable spectral match between laboratory analyses and remote sensing observations from Mercury has been obtained. However, we demonstrate that infrared spectroscopy is a rapid and nondestructive method to characterize mineral phases and thus an excellent tool for planetary surface characterization in space missions.

INTRODUCTION

Northwest Africa (NWA) 7325 was found in 2012 in Western Sahara, and comprises 35 pieces with a total mass of 345 g. The reported bulk rock Mg/Si (0.332) chemical ratio (Irving et al. 2013) and the low Fe content Mg# (molar [MgO]/[MgO+FeO]% × 100) ~97 (Kita et al. 2014) are similar to the chemical properties

of the upper few microns of Mercury's regolith, as mapped from orbit by the NASA MESSENGER mission X-ray fluorescence spectrometer (Weider et al. 2012). Based on this compositional similarity, Irving et al. (2013) suggested that the ungrouped achondrite NWA 7325 could potentially be a good candidate for a hermean meteorite and thus the first sample from the planet Mercury.

In the first petrological study of NWA 7325 the sample was described as a cumulate gabbro with a medium-grained plutonic igneous texture, which was presumably excavated from deeper within the parent body (Irving et al. 2013). Based on the existence of melt veins containing SiO_2-normative residual melts and zoned plagioclase, and the dissolution textures of pyroxene in plagioclase Bischoff et al. (2013) challenged the slow cooling model of Irving et al. (2013) and suggested that the present rock experienced fast cooling after a second (partial) melting event. Dominant mineral phases are calcic plagioclase (56 vol%), Cr-rich diopside (27 vol%), and forsterite (16 vol%) (Irving et al. 2013). Minor phases are sulfide (troilite), chromite, kamacite, taenite, and eskolaite (Irving et al. 2013), with an SiO_2 normative glass phase or late residual melt being present as well (Bischoff et al. 2013). Bulk rock studies have shown depletion in lithophile trace elements compared with lunar gabbroic/troctolitic meteorites, and a large positive Eu-anomaly, with low REE contents but elevated HFSE (high field strength elements, which are ordinarily incompatible in rock-forming minerals) contents (Irving et al. 2013). The oxygen isotopic composition is similar to that of ureilites and of various pieces from the Almahata Sitta meteorite, a complex polymict breccia containing chondritic and achondritic meteorite fragments (Horstmann and Bischoff 2014). In addition, like the ureilites and Almahata Sitta, olivines in NWA 7325 display elevated Cr- and Ca-contents (e.g., Weber et al. 2003; Horstmann and Bischoff 2014). However, the chromium isotopic composition of NWA 7325 is significantly different to that of the ureilites, which might be a hint that these meteorites may not come from a common parent body (Sanborn et al. 2013). Bulk sample U, Th, and Pb contents are extremely low in diopside, which is consistent with other meteorites that have a low degree of terrestrial alteration (Rocholl and Jochum 1993). NWA 7325 has a crystallization age of 4562.5 ± 4.4 Ma based on Pb dating analyses (Amelin et al. 2013). This age seems to be much too old for any terrain on Mercury's surface constrained by the absolute model crater counting method (Marchi et al. 2013). However, we note that the crater counting method for Mercury is still a model that is based on an extrapolated model from the lunar cratering curve.

In petrographic studies, plagioclase from NWA 7325 was characterized as "dull" or "turbid" due to either sulfide/metal particles or the assimilation of Ca-pyroxene (Bischoff et al. 2013; Irving et al. 2013). Signs of secondary melting events are recorded by plagioclase (e.g., remnants of twinning) and SiO_2-normative late residual melt in small veins. In addition, a low degree of shock metamorphic overprint is marked by olivine (S2—very weakly shocked, shock pressure: 5–10 GPa; Stöffler et al. 1991) and magnesiochromite. Therefore, a second partial melting event, followed by fast cooling was suggested by Bischoff et al. (2013). All the above features indicate that NWA 7325 is a unique sample and unlike any other known achondrite.

Here, we present a more detailed petrological and cosmochemical study, including high precision trace element data that provide new insights on the evolution of NWA 7325. In addition, xenon and oxygen isotopic data for NWA 7325 are presented. Xenon isotopes are tracers of input from volatile reservoirs. Radioactive decay of (now extinct) ^{129}I (half-life ~16 Ma) and ^{244}Pu (half-life ~82 Ma) during the first few 100s of million years of the solar system produced xenon of distinct isotopic compositions. Thus, these isotopes may provide further constraints on the history of this ancient rock. Argon isotopes likewise record the timing of thermal events and the cosmogenic exposure history of the meteorite prior to delivery to the Earth. Oxygen isotopes give key information that can be used to relate the parent body of NWA 7325 to that of other compositionally similar meteorite groups. Raman spectroscopy helps to identify and characterize shock induced deformation in some minerals. Furthermore, we provide the first mid-infrared spectra of the sample that can be compared with the available data from ground-based spectral observations of Mercury.

Infrared spectroscopy is a well-known and powerful technique to investigate mineral phases quickly and nondestructively. The mid-infrared spectrometer (MERTIS—Mercury Radiometer and Thermal Infrared Spectrometer) will be one of the instruments on the joint ESA/JAXA mission BepiColombo (Hiesinger et al. 2010; Rothery et al. 2010). BepiColombo, to be launched in 2016, will reach Mercury in 2024 (Benkhoff et al. 2010).

MERTIS onboard BebiColombo's Mercury Planetary Orbiter (MPO) consists of a thermal infrared spectrometer and a thermal infrared radiometer. It will investigate the following key areas (Hiesinger et al. 2010):

1. Christiansen features (CF—visible in the IR spectra as a minimum between 7.5 μm and 9 μm only for silicates) and Reststrahlen bands (RB—visible in the

IR spectra in the longwave range following the CF) of minerals on the surface;
2. The mineralogy of the surface of Mercury (plagioclase, pyroxenes, sulfides, sulfates);
3. The presence of elemental sulfur.

So far, two spacecraft (Mariner 10 and MESSENGER) have visited Mercury and conducted a wide range of observations of its surface and near-surface environment. In particular, MESSENGER data demonstrate a low-iron composition for the surface of Mercury, suggesting that the core is iron-rich. It showed that the surface consists of a mix of smooth plains, older intercrater plains, and more heavily cratered areas (Izenberg et al. 2014). Mercury, with a diameter of only 4878 km, is the smallest of the terrestrial planets. Due to its proximity to the Sun, it is also the least optically investigated planet. Therefore, obtaining more information about Mercury is a key to improving our understanding of processes in the early solar system, including the formation of the terrestrial planets.

In order to enable proper interpretation and to optimize instrumentation during its development a knowledge base for Mercury is necessary, including the potential mineralogy of its surface. Unfortunately, in contrast to the Moon or Mars, so far no meteorite samples have been unambiguously identified to be descended from Mercury. Meteorites derived from the crust of Mercury should have low concentrations of Fe to match recent data collected by the MESSENGER mission (Nittler et al. 2011; Weider et al. 2012, 2014). The surface of this planet likely is dominated by the pyroxene (enstatite and diopside), plagioclase, and sulfide (Burbine et al. 2002; Stockstill-Cahill et al. 2012; Weider et al. 2012, 2014; Vaughan and Head 2014). Our initial spectroscopic examination of NWA 7325 was undertaken on the basis that it represented a plausible sample from Mercury. While other lines of evidence outlined above suggest that NWA 7325 is not from Mercury, the results of our spectral study indicate that it does display a good match to MESSENGER data (Helbert et al. 2013; Morlok et al. 2013). While such a match cannot confirm or disprove the suggestion that NWA 7325 may be from Mercury, it does mean that NWA 7325 presently provides the best opportunity to improve and augment our existing database of infrared spectra in preparation for the upcoming MERTIS data set.

TECHNIQUES

We applied a wide range of analytical techniques to study NWA 7325. For light and electron microscope investigations, as well as for Raman and some Fourier transform infrared spectroscopy measurements the same polished thin section (PL-13022) was used. This thin section was polished with sintered diamond grinding wheels and ethanol. For all other investigations grains were hand-picked from the gently crushed bulk sample. Further details about sample processing are discussed below.

Light and Electron Microscopy

Overview images of the entire sample, of smaller pieces, and of the thin section were obtained with a KEYENCE Digital Microscope VHX-500F. A Zeiss Axiophot optical microscope with transmitted and polarized light was used for a preliminary characterization of the thin section.

After the thin section was carbon coated, a montage whole sample backscatter electron (BSE) image, elemental maps, and high-quality BSE images were collected using a JEOL JSM-6610LV scanning electron microscope (SEM) at the ICEM (Interdisciplinary Center for Electron Microscopy and Microanalysis)/Institut für Planetologie. In addition, initial compositional analyses were carried out with the SEM at an accelerating voltage of 20 kV. Detailed quantitative analyses of all minerals were made using a JEOL JXA-8900 Superprobe electron probe microanalyzer (EPMA) at ICEM/Institut für Mineralogie equipped with four wavelength-dispersive spectrometers and operating at an excitation voltage of 15 kV, a beam current of 15 nA, and a beam size of ~1 μm. Corrections for matrix effects were made using the $\Phi\rho(z)$ procedure of Armstrong (1991). Natural and synthetic USNM (United States National Museum; now National Museum of Natural History, Smithsonian Institution, Washington, DC) standards were used for standardization (Jarosewich et al. 1980). Mineral compositions were checked for stoichiometry and only those with analytical totals between 99–100.5 wt% were used.

Mid-Infrared Spectroscopy

Bulk measurements were made using a Bruker Vertex 70v at the IR/IS laboratory of the Institut für Planetologie in Münster. All analyses were collected using identical incidence and emergence angles (30°/30°) using a Bruker A513 biconical reflectance stage. For each individual spectrum, 512 scans were accumulated in the wavelength range from 2 to 25 μm. All reflectance analyses were made at low pressure (10^{-3} bar).

A sample (aliquot of ~3 g) of NWA 7325 was crushed and dry-sieved to obtain size fractions from

0–25, 25–63, 63–125, and 125–250 μm. The powders were loaded into aluminum cups (1 cm diameter) and gently flattened using a spatula for analysis. To remove the instrumental background, we used a diffuse gold standard, against which the sample spectra were ratioed. The resulting spectra are presented in absolute reflectance.

In addition, the polished thin section was also analyzed, using an aperture of 4 mm. In this case a polished gold mirror was used as background. Individual phases in the sections were investigated using a Perkin Elmer Spotlight 400 FTIR Imaging System at the School of Earth, Atmospheric, and Environmental Science (SEAES), The University of Manchester. Individual spots on the polished section were analyzed under ambient pressure, using aperture sizes from 25 × 25 μm and 50 × 50 μm. Grain orientation is a potential problem in the in situ FTIR analysis of mineral grains in thin sections. In order to avoid orientation effects a series of spectra from different grains was obtained, wherein 128 individual spectra of the same spot were accumulated for each spectrum. The spectra were normalized to the strongest feature in the 7–14 μm range and averaged to one spectrum. However, if a sample has a general preferred grain orientation the resulting spectra could be affected (Stephen et al. 2010). The spectra from the polished section are presented in relative abundance. To confirm the phases, we compared the spectral features to reference data from the Johns Hopkins University Spectral Library (ASTER Database; Baldridge et al. 2009).

Raman Spectroscopy

Raman measurements were performed on the uncoated thin section with a confocal HORIBA Jobin Yvon LabRam HR-800 Raman microscope at the Institut für Physikalische Chemie in Münster. A frequence doubled Nd:YAG laser (wavelength= 532 nm), with a power of ~5 mW was used for excitation. A 50× objective was used with a charged-coupled device (CCD) detector after dispersion by a grating of 600 grooves mm^{-1}. Measurements were conducted using a grating of 1800 grooves mm^{-1}. A silicon wafer (520.7 ± 0.5 cm^{-1}) was applied for calibration. An 800 mm focal length guaranteed a good spectral resolution. Furthermore, an edge filter was used, for measuring the exact Stokes lines. The data interpretation procedure used a Gaussian fit to find the exact position of the maximum of each peak. Minerals were identified by comparing the band positions in our spectra with those of the appropriate minerals in the RRUFF database (Downs 2006).

Xenon and Argon Isotopic Analysis

The xenon isotopic signature of a single, 1.67 mg sample of NWA 7325 was analyzed using the RELAX (Refrigerator Enhanced Laser Analyser for Xenon) mass spectrometer at The University of Manchester (Gilmour et al. 1994; Crowther et al. 2008). This sample comprised ~11 small grains of bulk rock. The sample was step heated with a continuous wave Nd:YAG laser (λ = 1064 nm), for 1 min at a series of sequentially increasing laser powers. The gas extracted in each step was gettered (sintered Zr, ~350 °C) in order to remove active gases, before being admitted into the mass spectrometer. Gas in the mass spectrometer continuously condenses on a localized cold spot. Pulses from an infrared laser (λ = 1064 nm, 5 mJ, 10 ns pulse) release gas from the cold spot every 0.1 s. The ionizing laser (λ = 249.6 nm, 2 mJ) is then fired through the resulting plume of gas when its concentration reaches a maximum in the ionizing region, selectively ionizing xenon. The xenon isotopes are separated according to their mass in the time of flight mass spectrometer and a microchannel plate detector (MCP) allows the detection of all xenon isotopes from each laser pulse.

Data were acquired from 3000 consecutive cycles of the condensation-release-ionization process over a period of 5 min. Isotope ratios and the signal intensity of a normalizing isotope were calculated by extrapolation back to the inlet time. Sample analyses were interspersed with air calibrations and procedural blanks. Air calibrations enable a correction to be made for instrument-dependent mass fractionation and for the absolute quantities of gas to be calculated. The procedural blank, which was ~2500 atoms ^{132}Xe during these analyses, made negligible contributions to the quantities of gas measured from the samples in these analyses. Thus, a blank correction of our data has not been applied.

^{40}Ar-^{39}Ar age determinations were performed using stepped laser heating of a bulk sample (3.49 mg), a plagioclase separate (2.27 mg), and a pyroxene separate (1.4 mg). Minerals were identified from a crushed bulk sample and picked using optical microscopy. Samples were irradiated at the Oregon State University Radiation Center. Aliquots of Hb3gr monitor (1080.4 ± 1.1 Ma; Renne et al. 2010) were positioned in close proximity (few mm) to the samples which were irradiated in silica glass vials. The J value, a parameter that is representative of the neutron irradiation conditions, was 0.08089 ± 0.00097 (1σ) (where this error used in the age calculation does not take into account the uncertainty on the monitor age). Stepped heating was performed using a Photon Machines Fusions IR 10.6 μm wavelength CO_2 laser coupled to a

Thermo Scientific™ Argus VI preparation bench and multicollector mass spectrometer. The sample was lased using a 3 mm defocused beam for 30 s with increasing watt output power at each step (see Table 4 for details) until the sample was degassed. The released gas was cleaned for two minutes on a hot getter, and then 1 min on a hot and cold getter prior to introduction to the mass spectrometer. Isotopes were measured simultaneously and in peak jumping mode: ^{40}Ar, ^{38}Ar, and ^{37}Ar were measured on faraday cups and ^{39}Ar and ^{36}Ar on a Compact Discrete Dynode (CCD) detector. Data have been corrected for blank contribution, mass discrimination, neutron-induced interference isotope production on ^{40}Ar, ^{39}Ar, ^{38}Ar, and ^{36}Ar and decay of ^{37}Ar and ^{39}Ar and using the decay constants of Renne et al. (2010). ^{40}Ar-^{39}Ar ages are reported at the two standard deviation (2σ) level of uncertainty. We note that the uncertainties on reported ^{40}Ar-^{39}Ar ages are large due to the high CaO and low K_2O wt% composition of the mineral phases and bulk rock analyzed requiring a large correction for calcium-derived ^{39}Ar. Exposure ages were calculated using the ratio of cosmogenic ^{38}Ar (Hennessy and Turner 1980) to the concentration of ^{37}Ar (as a measure of sample Ca composition derived from this study and the bulk rock composition reported by Irving et al. 2013). $^{38}Ar_c/^{37}Ar$ ratios then provide apparent cosmic ray exposure (CRE) ages using the sample chemistry and 4π cosmogenic production rates of Eugster (1988). The Isoplot v4 (after Ludwig 2012) Excel plugin was used to produce data plots.

Oxygen Isotopes

Oxygen isotope analysis of NWA 7325 was carried out at the Open University using an infrared laser-assisted fluorination system (Miller et al. 1999). A 110 mg sample of NWA 7325, consisting of clean interior fragments, was crushed and homogenized and the sample chamber of the oxygen line was loaded with approximately 2 mg aliquots, along with silicate standards (Miller et al. 1999). Oxygen was released from the samples by heating in the presence of BrF_5. After fluorination, the released oxygen gas was purified by passing it through two cryogenic nitrogen traps and over a bed of heated KBr. The oxygen gas was analyzed using a MAT 253 dual inlet mass spectrometer. Published analytical precision (2σ) for our system, based on replicate analysis of international (NBS-28 quartz, UWG-2 garnet) and internal standards, is approximately ±0.08‰ for $\delta^{17}O$; ±0.16‰ for $\delta^{18}O$; ±0.05‰ for $\Delta^{17}O$ (Miller et al. 1999). Changes to analytical procedures implemented subsequent to the system description given by Miller et al. (1999) have resulted in improvements to precision such that 39 analyses of our internal obsidian standard undertaken during six separate sessions in 2013 gave the following combined results: ±0.05‰ for $\delta^{17}O$; ±0.09‰ for $\delta^{18}O$; ±0.02‰ for $\Delta^{17}O$ (2σ). The accuracy (1σ) quoted for NWA 7325 is based on replicate analyses.

Oxygen isotopic analyses are reported in standard δ notation, where $\delta^{18}O$ has been calculated as: $\delta^{18}O = ([^{18}O/^{16}O]_{sample}/[^{18}O/^{16}O]_{ref} - 1) \times 1000$ (‰) and similarly for $\delta^{17}O$ using the $^{17}O/^{16}O$ ratio, the reference being VSMOW: Vienna Standard Mean Ocean Water. $\Delta^{17}O$, which represents the deviation from the terrestrial fractionation line, has been calculated as: $\Delta^{17}O = \delta^{17}O - 0.52 \times \delta^{18}O$.

High Precision Trace Element and Sr Isotope Measurements

High precision trace element measurements by isotope dilution were carried out on a ~85 mg aliquot of a 1 g split from NWA 7325. Elements measured include the high field strength elements W, Nb, Ta, Zr, Hf; the rare earth elements Nd, Sm, and Lu; as well as Rb-Sr using mixed ^{183}W-^{180}Ta-^{94}Zr-^{180}Hf-^{176}Lu- ^{149}Sm-^{150}Nd isotope tracers. Analytical procedures for HFSE and REE are outlined in detail by Münker et al. (2001) and Münker (2010), those for Sr by Kirchenbaur et al. (2012), and those for Rb by Nebel et al. (2005). In general, after digestion in a 1:1 HF-HNO_3 mixture, the elements of interest were separated by ion exchange chromatography, to avoid polyatomic and isobaric interferences, using Triskem Ln Spec, AG 1 X-8, and AG 50W X8 resins. Isotope dilution measurements were performed using the Thermo Neptune MC-ICPMS at the joint Cologne-Bonn facility, where the Nb concentration was measured as Zr/Nb relative to the Zr/Nb composition of 99.9% pure mixed AMES metal standards and the Zr composition determined by isotope dilution. The $^{87}Sr/^{86}Sr$ measurement for NWA 7325 is normalized relative to a $^{86}Sr/^{88}Sr$ value of 0.1194 using the exponential law and reported relative to a value of 0.710240 for NBS 987 (measured average value in the same analytical session: 0.710229). Procedural blanks were 8 pg for W, 15 pg for Nb, 16 pg for Ta, 642 ng for Zr, 25 pg for Hf, 60 pg for Rb, 165 pg for Sr, 50 pg for Nd, 20 pg for Sm, and 6 pg for Lu. Typical external uncertainties (2σ) are ~ ±1% for all element concentrations except for Nb (±4%). Typical external reproducibility for $^{176}Lu/^{177}Hf$ and $^{147}Sm/^{144}Nd$ are 0.2%, those for $^{87}Rb/^{86}Sr$ are ±1% (2σ). The somewhat larger uncertainties listed in Table 5 originate from propagated blank uncertainties assumed to be ±50%. The propagated external error for the $^{87}Sr/^{86}Sr$ measurement reported here is

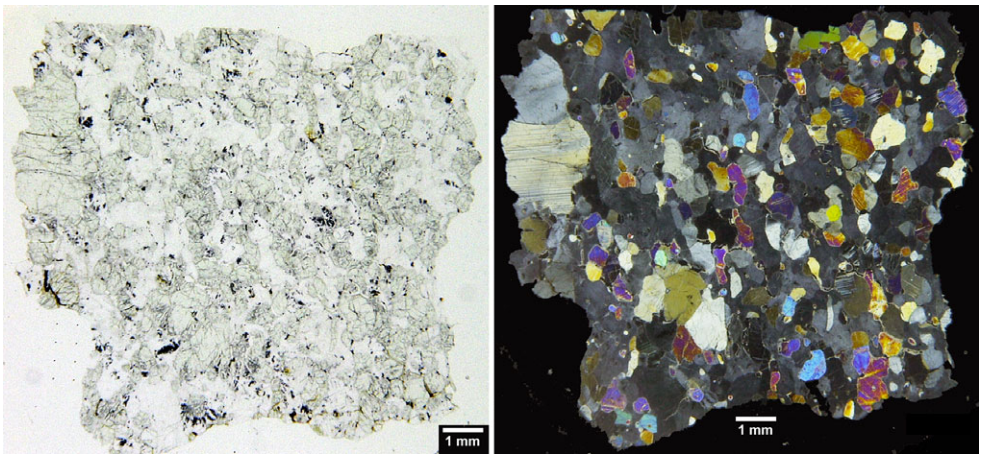

Fig. 1. Overview image of the investigated thin section in plane-polarized light (left) and between crossed polarizer (right) (gray phase: mostly plagioclase; colored phases: pyroxene and olivine).

±0.000070 (2σ), also including the propagated error from spike subtraction.

RESULTS

Mineralogical results are given in the Mineralogical Results section and in Figures 1–5. Detailed qualitative investigations and the results of quantitative chemical analyses of the main minerals plagioclase, pyroxene, and olivine obtained with EPMA and SEM are listed in Tables 1 and 2. The infrared and Raman results, as well as results of the xenon, argon, and oxygen isotope investigations, and the trace element measurements are presented in the Fourier Transform Infrared Spectroscopy, Raman Spectroscopy, Xenon and Argon Isotopic Composition, Oxygen Isotope Results, High Precision Trace Element, and Sr Isotope Measurements sections; Tables 3–5; and Figures 6–14.

Mineralogical Results

The polished thin section of NWA 7325 reveals it to be a relatively coarse-grained sample (Fig. 1), which consists of plagioclase-rich domains (approximately ~54 vol%). These domains appear dull (sometimes nearly opaque) or "turbid" in plane-polarized light (Fig. 2a). This appearance is mainly caused by abundant tiny sulfide and metal particles (compare Fig. 2b). At the grain boundaries between Ca-pyroxene and plagioclase, the dissolution of pyroxene is visible (Fig. 2c). Tiny sulfide and metal particles are also observed scattered throughout the plagioclase and Ca-pyroxene. No low-Ca-pyroxene has been observed.

The anorthite content of the plagioclases varies between An_{79}–An_{94}. Table 1 and some grains show remnants of twinning-like features (Fig. 2d). In addition, a second generation of plagioclase is observed on grain boundaries, around the mafic minerals, between Ca-pyroxene, and within Ca-pyroxenes (probably on pre-existing cracks) (Fig. 2e). This secondary plagioclase contains significantly more Na (up to ~Ab_{30}) and exhibits lath-like shapes indicating crystallization from a melt. An SiO_2-normative late residual melt (Figs. 2g and 2h) was occasionally found within these areas. Overall the main plagioclase is still birefringent and not shocked to maskelynite.

Olivine in the investigated thin section occurs as a minor phase at ~2 vol% and has an equilibrated forsteritic composition (Fa <3; Table 2). NWA 7325 has exceptionally low MnO compared with mafic minerals in other achondritic meteorites. The FeO/MnO versus Mg# ratio trends in olivine (Fig. 4) are consistent with accumulation from a subchondritic source region and show that NWA 7325 is unique compared with other achondritic meteorite classes. The high Ca and Cr concentrations (Table 2) are comparable to those of ureilites and Almahata Sitta (e.g., Weber et al. 2003; Horstmann and Bischoff 2014). Olivine grains show undulatory extinction and irregular fractures (Fig. 2f) suggesting that they are only very weakly shocked to a shock level of S2 (following the scheme of Stöffler et al. 1991).

Pyroxene crystals, which show no mechanical twinning or undulatory extinction, comprise 44 vol% of the investigated thin section (Fig. 1). Cr-diopside ($En_{53}Wo_{46}$ [Table 2]) has a chromium content of around 1 wt% (Table 2). Crystals of pyroxene are often cross cut by fractures (Fig. 2f).

Minor phases in the investigated thin section include Fe-sulfide, magnesiochromite, magnetite, and taenite. In most instances these grains are associated and found in contact with each other (Fig. 5). Finally,

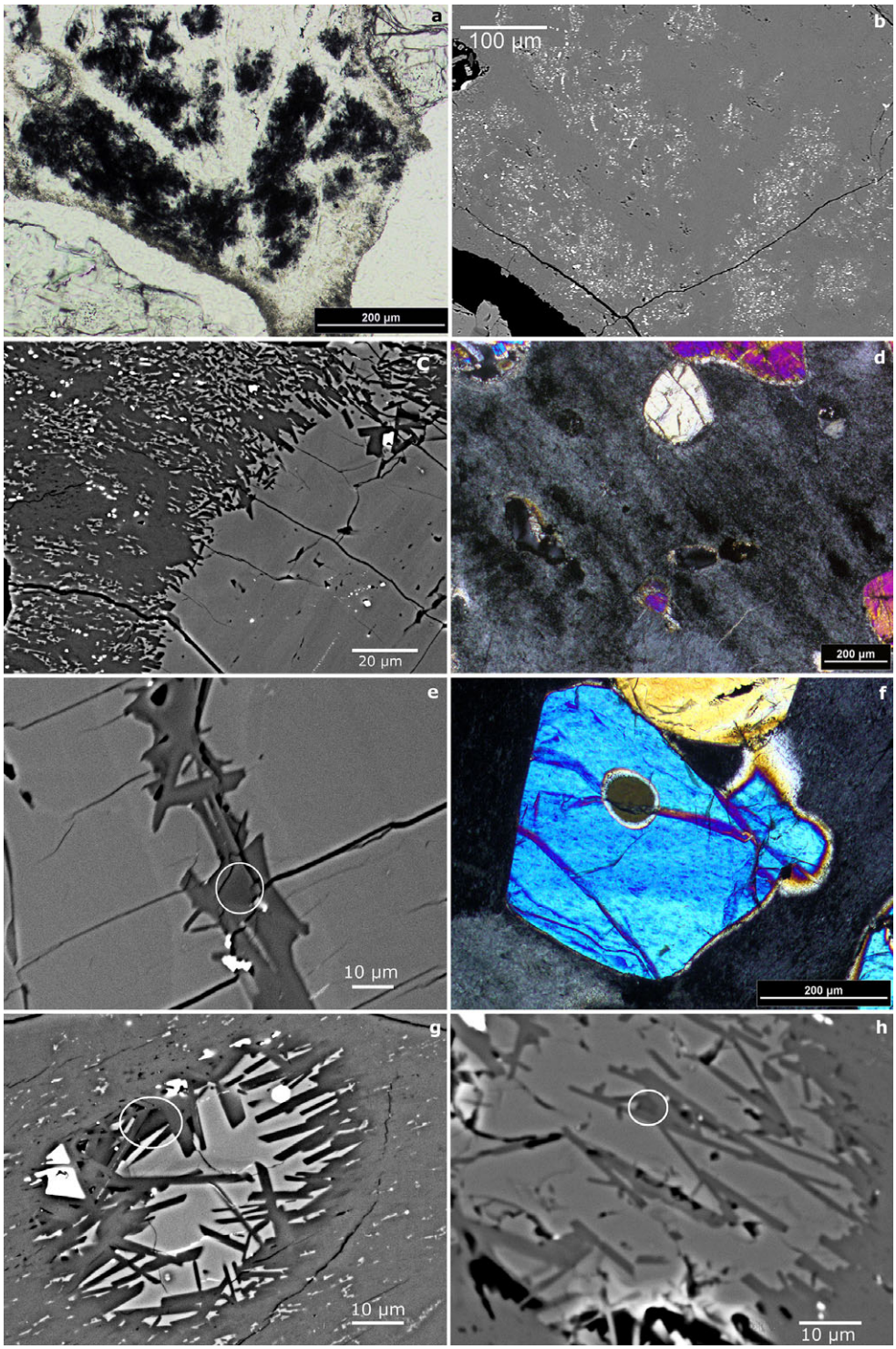

Fig. 2. a) Optical microscope image of plagioclase domains showing a nearly opaque appearance. b) BSE image of these "turbid" looking domains indicating tiny sulfide and metal particles. c) BSE image of a contact between Cr-diopside (light gray) and plagioclase (dark gray) showing the dissolution of pyroxene. d) Light microscope image with crossed polarizer of a plagioclase showing twinning remnants. e) BSE image of secondary plagioclase. Circle: area with a high amount of Na (Ab_{30}). f) Light microscope image with crossed nicols of an olivine showing undulatory extinction and irregular fractures. g, h) BSE image showing the resorption of Ca-pyroxene and fast crystallization of plagioclase laths. SiO_2-normative late residual melt marked by circles.

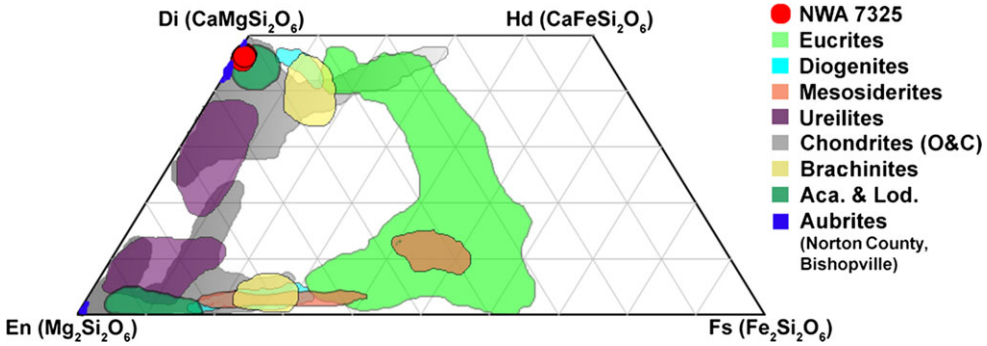

Fig. 3. Pyroxene quadrilateral detailing the composition of pyroxene in NWA 7325 (red circles) compared with chondrite (data from Berlin 2009) and achondrite meteorite groups (brachinite and brachinite-like achondrites: Corder et al. 2013; acapulcoites (Aca.) and lodranites (Lod.): Corder et al. 2013; ureilites: Warren and Rubin 2010; mesosiderites: Nehru et al. 1980; diogenites and eucrites: McSween et al. 2011, aubrites: own measurements with the EPMA).

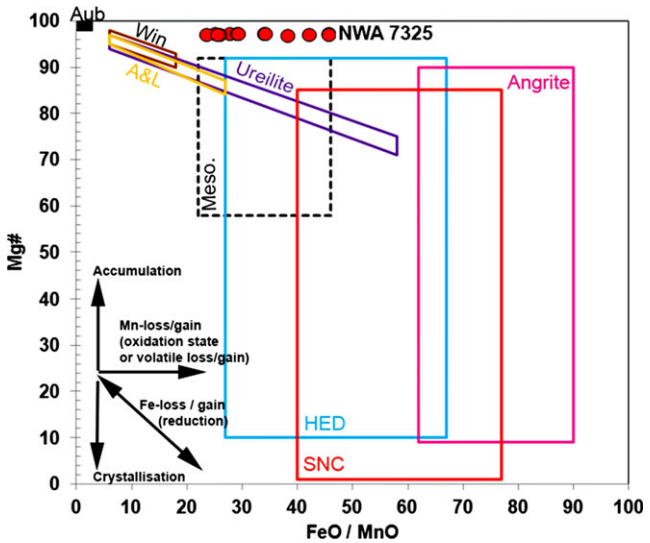

Fig. 4. Olivine FeO/MnO ratio versus Mg# of olivine in NWA 7325 compared with olivine in other achondritic meteorite groups where the approximated fields are summarized from literature data (SNC meteorites [Mars]: Sarbadhikari et al. 2011; HED meteorites [Vesta]: Takeda et al. 1984; Ikeda and Takeda 1985; angrites: Brearley and Jones 1998; mesosiderites [Meso.]: Nehru et al. 1980; ureilites: Downes et al. 2008; winonaites [Win]: Benedix et al. 2005; acapulcoites and lodranites [A&L]; McCoy et al. 1996, 1997; aubrites [Aub]: Brearley and Jones 1998).

calcite was found as rims and along grain boundaries (Fig. 5, middle) and most probably formed as a terrestrial weathering product, similar to calcite occurrences in other hot desert meteorites (Stelzner et al. 1999; Lee et al. 2006).

Fourier Transform Infrared Spectroscopy

Microspectroscopy

In Fig. 6a the average of 28 pyroxene spectra obtained using an aperture of 50 × 50 μm is presented. Notable characteristics include the CF at 8.44 μm and strong RB at 9.01, 10.37, and 10.84 μm. Weaker bands are at 10.0, 10.55, and ~14.8 μm. These are very similar to the band positions for Ca-pyroxenes (Hamilton 2000).

First generation anorthite spectra averaged from 34 spectra using an aperture of 50 × 50 μm show a CF at 8.13 μm. Strong RB are found at 8.72, 8.96, 10.75, 13.26, 13.78, and 15.0 μm. These bands are identical to analyses of anorthite reference material (Baldridge et al. 2009), except for the lack of a feature at 9.7 μm in the NWA 7325 anorthite. The average of 13 olivine grains has a CF at 8.77 μm. Further characteristic bands are observed at 9.49, 10.13, 10.51, and 11.94 μm. This is typical for forsteritic olivine (e.g., Hamilton 2010).

The nature of fracture infillings was investigated with the FTIR microscope. The average of three spectra collected using a 25 × 25 μm aperture show a CF at 6.27 μm. Strong RB are located at 7.08 μm, 11.47 μm, and 14.1 μm. The features are similar to those found in calcite (Baldridge et al. 2009), but are shifted to higher wavelengths. This could point to similar carbonates but with some variation in chemical composition.

Spectroscopy of Powders From Bulk Samples

The four grain size fractions 0–25 μm, 25–63 μm, 63–125 μm, and 125–250 μm result in reflectance spectra that have similar band positions (Fig. 6b). A CF is present at 8.1–8.3 μm. RB are at 9.0 μm, 9.2–9.3 μm, 10.6 μm, and 10.8 μm, with a shoulder at 9.8 μm. Further strong bands are at ~15.9 μm. The feature of the carbonate-rich vein fillings is possibly visible at ~6.9 μm, confirming observations of terrestrial weathering in BSE images (Fig. 5) and Raman data (Fig. 8b).

The RB for the finest grain size fraction (0–25 μm) is identical to that for the size fractions > 25 μm, but

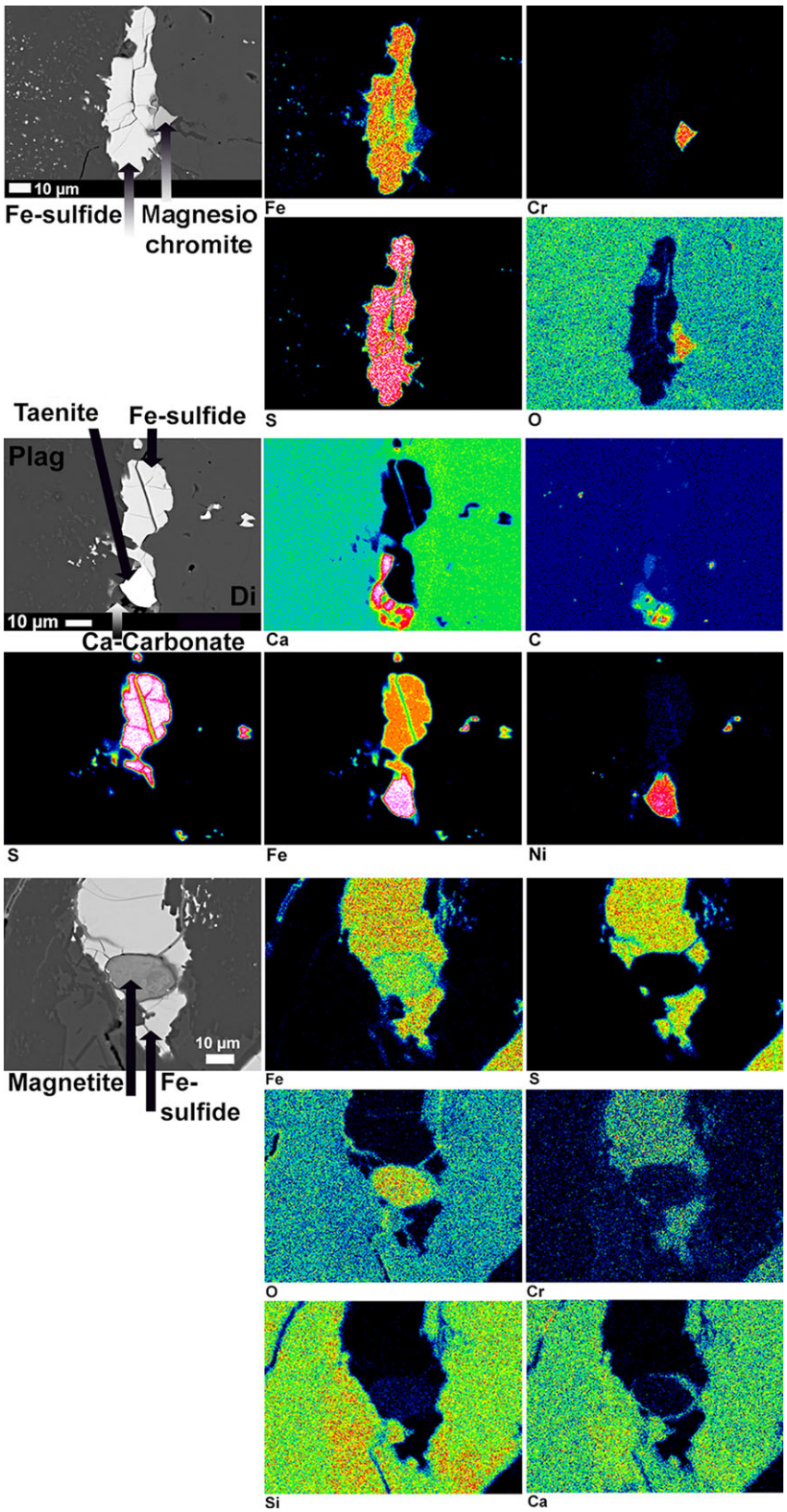

Fig. 5. Element maps of three areas with different minor phases. The BSE images of the investigated areas are shown on the left-hand side. Top: Fe-sulfide and magnesiochromite between plagioclase (left) and diopside (right). Middle: Taenite, Fe-sulfide, and calcite between plagioclase and diopside. Bottom: Magnetite bleb surrounded by Fe-sulfide within the silicates.

Table 1. Representative EPMA and SEM (in italics) analyses in weight% of 8 plagioclases and anorthite (An) and albite (Ab) content in mole% (n.d. = not detected)

SiO_2	46.4	46.2	47.0	44.0	44.5	48.5	*49.2*	*50.1*
Al_2O_3	34.6	34.3	32.0	35.7	34.5	32.0	*32.4*	*32.0*
CaO	17.7	17.9	18.6	17.5	18.8	16.3	*14.9*	*13.9*
Na_2O	1.22	1.11	1.22	1.00	0.73	2.34	*2.72*	*3.3*
K_2O	n.d.	<0.01	<0.04	n.d.	n.d.	<0.01	*0.04*	*0.02*
MgO	0.47	0.40	0.39	0.62	0.41	0.19	*0.39*	*0.34*
MnO	0.05	0.06	0.07	0.05	<0.03	<0.02	*0.07*	*n.d.*
Cr_2O_3	<0.02	n.d.	<0.03	0.07	<0.04	n.d.	*0.13*	*0.17*
FeO	0.06	0.08	0.07	0.08	<0.01	0.19	*0.19*	*0.24*
Total	100.52	100.06	99.42	99.02	98.97	99.54	*100.04*	*100.07*
An	88.9	89.8	89.2	90.6	93.5	79.3	*75.0*	*70.1*
Ab	11.1	10.1	10.6	9.4	6.5	20.7	*24.8*	*29.8*

Table 2. Average EPMA analyses in weight% of 12 representative Cr-diopsides (left row) and 12 representative olivines (right row); enstatite (En), wollastonite (Wo), forsterite (Fo), and fayalite (Fa) content in mole%; (n.d. = not detected).

SiO_2		53.7		42.0
MgO		18.6		54.0
FeO		0.69		2.60
CaO		22.6		0.32
MnO		0.06		0.09
Al_2O_3		2.71		0.04
Na_2O		0.17		<0.02
K_2O		n.d.		n.d.
Cr_2O_3		1.00		0.37
Total		99.53		99.44
	En	52.83	Fo	97.37
	Wo	46.06	Fa	2.63

with a much lower intensity. The smallest grain size fraction shows a transparency feature at 12.34 μm, which is not present in the spectra for the larger grain sizes. The spectra from bulk and powered samples represent a mixture mainly consisting of anorthite and diopside bands, with no clear olivine bands. The CF of the powders at 8.1–8.3 μm shows the dominance of anorthite, but the CF of diopside is still recognizable as a weak shoulder at 8.5 μm. The results are similar to those described by Helbert et al. (2013).

A spectrum collected from a polished thin section over an area of 4 × 4 mm and thus resembling a bulk measurement, shows features similar to those taken from the larger grain size fractions, but with a much higher intensity (Fig. 6b).

Raman Spectroscopy

A representative suite of Raman spectra obtained from the thin section of NWA 7325 are given in Figs. 7 and 8.

Raman spectra of feldspar can be separated into five main groups (Freeman et al. 2008), each of which is characteristic of individual feldspathic endmembers. The spectral regions are: Group I between 450–520 cm^{-1}, Group II 200–400 cm^{-1}, Group III below 200 cm^{-1}, Group IV between 600–800 cm^{-1}, and Group V between 900–1200 cm^{-1}. The plagioclase in NWA 7325 shows, in general, a slight decreasing signal/noise ratio due to spectra background enhancement and band broadening. The strongest features at 486 cm^{-1} and 505 cm^{-1}, and the third band of the Group I triplet at ~466 cm^{-1}, which is not resolved in high-temperature anorthite, provide evidence of a low-temperature primitive anorthite (low-T anorthite-*P*) feldspar (Fig. 7a). These lines can be ascribed to a mixed Si-O-Si/Al bending and stretching mode (Mernagh 1991). A second region below 450 cm^{-1} (Group II and III) is assigned to an external lattice mode (Mernagh 1991). Within this region, the investigated anorthite exhibits shifts at 285 cm^{-1}, 196 cm^{-1}, and 185 cm^{-1}. These shifts are also typical for low-T anorthite-*P* feldspar. The last strong shift at 557 cm^{-1} is also an IR active mode and is caused by tetrahedral deformation (McKeown 2005; Freeman et al. 2008).

The pyroxene is also identified as diopside by Raman measurements (Fig. 7b). A typical pyroxene spectrum is subdivided into three main regions (Huang et al. 2000). Peaks below 500 cm^{-1} are assigned to the stretching of nontetrahedral cation versus oxygen (Tribaudino et al. 2012). We detected Raman shifts at these frequencies that are characteristic of diopside at: 231 cm^{-1}, 329 cm^{-1}, and 395 cm^{-1}. The next peak at 668 cm^{-1} is assigned to chain Si-O stretching (Huang et al. 2000). Finally, the Stokes peak at 1012 cm^{-1} is the T-O stretching peak (Tribaudino et al. 2012). If we combine these results with the description of Wang et al. (2001), who compared the structural and compositional features of pyroxenes with each other, the Cr-diopside is most likely a pyroxene with $C2_1/c$

Table 3. ^{132}Xe concentrations and xenon isotopic ratios measures in NWA 7325.

Laser current (A)	^{132}Xe ($\times 10^{-12}$ cm^3 STP g^{-1})	^{124}Xe/^{132}Xe	^{126}Xe/^{132}Xe	^{128}Xe/^{132}Xe	^{129}Xe/^{132}Xe	^{130}Xe/^{132}Xe	^{131}Xe/^{132}Xe	^{134}Xe/^{132}Xe	^{136}Xe/^{132}Xe
11.0	0.06 (1)	n.d.	0.0574 (367)	1.393 (280)	0.67 (18)	n.d.	0.564 (159)	0.457 (145)	0.265 (113)
11.5	0.22 (2)	n.d.	0.0120 (93)	0.378 (51)	0.95 (12)	0.116 (33)	0.661 (89)	0.398 (65)	0.273 (53)
12.0	0.41 (2)	0.001 (1)	0.0082 (48)	0.350 (31)	1.03 (8)	0.173 (24)	0.796 (63)	0.412 (42)	0.321 (36)
12.5	0.65 (3)	n.d.	0.0033 (31)	0.189 (17)	1.07 (6)	0.164 (19)	0.819 (53)	0.378 (32)	0.316 (29)
13.0	1.35 (4)	0.009 (5)	0.0026 (14)	0.104 (8)	1.13 (5)	0.175 (14)	0.814 (37)	0.381 (22)	0.311 (20)
13.5	1.32 (4)	0.001 (3)	0.0047 (17)	0.115 (8)	1.19 (5)	0.147 (12)	0.788 (34)	0.368 (21)	0.296 (18)
14.0	5.44 (6)	0.004 (1)	0.0030 (5)	0.063 (3)	1.26 (2)	0.177 (5)	0.829 (14)	0.382 (8)	0.313 (7)
14.5	4.33 (6)	0.007 (2)	0.0025 (6)	0.065 (3)	1.29 (2)	0.167 (6)	0.827 (17)	0.378 (10)	0.302 (9)
15.0	3.03 (6)	0.005 (2)	0.0034 (9)	0.069 (4)	1.31 (3)	0.163 (8)	0.806 (22)	0.367 (13)	0.294 (12)
15.5	8.51 (7)	0.007 (1)	0.0023 (4)	0.055 (2)	1.32 (2)	0.166 (4)	0.812 (10)	0.371 (6)	0.295 (5)
15.7	8.38 (3)	0.001 (5)	0.0051 (21)	0.068 (7)	1.39 (6)	0.170 (15)	0.813 (39)	0.373 (24)	0.300 (20)
15.9	3.13 (4)	0.008 (2)	0.0033 (6)	0.062 (3)	1.44 (2)	0.162 (6)	0.841 (16)	0.383 (9)	0.325 (9)
16.1	2.33 (4)	0.008 (2)	0.0032 (8)	0.079 (4)	1.47 (3)	0.164 (7)	0.810 (19)	0.383 (11)	0.317 (10)
16.3	0.83 (3)	0.007 (6)	0.0029 (21)	0.142 (11)	1.39 (6)	0.156 (14)	0.793 (38)	0.385 (24)	0.291 (20)
16.5	0.76 (3)	0.008 (8)	0.0059 (25)	0.154 (13)	1.43 (7)	0.123 (14)	0.800 (45)	0.381 (28)	0.299 (24)
17.0	0.61 (2)	n.d.	0.0069 (25)	0.114 (9)	1.37 (5)	0.151 (13)	0.750 (34)	0.374 (22)	0.314 (20)
20.5	6.28 (4)	0.006 (1)	0.0024 (3)	0.054 (2)	1.47 (1)	0.170 (3)	0.817 (9)	0.379 (5)	0.322 (5)
20.5 repeat	0.19 (1)	n.d.	0.0146 (78)	0.280 (32)	1.32 (11)	0.132 (3)	0.777 (75)	0.352 (45)	0.275 (39)
Total	40.27 (17)								

Numbers in parentheses represent 1 standard deviation uncertainties in the units of the last significant figure quoted.
Isobaric hydrocarbons intender with the ^{126}Xe and ^{128}Xe peaks in the mass spectrum, contributing additional uncertainty to these ratios.
The lowest temperature heating step released only a very minute amount of gas, and this step is essentially blank.

Table 4. NWA 7325 ^{40}Ar-^{39}Ar analytical data calculated from each heating release step. Errors are given at the 2s level of uncertainty, n.d. = not determinable.

	Concentration (moles)												
Laser power (W)	^{36}Ar ($\times 10^{-18}$)	^{37}Ar ($\times 10^{-18}$)	^{38}Ar ($\times 10^{-18}$)	^{39}Ar ($\times 10^{-18}$)	^{40}Ar ($\times 10^{-18}$)	Cl ($\times 10^{-12}$)[a]	K ($\times 10^{-12}$)[b]	Ca ($\times 10^{-12}$)[c]	Cum. ^{39}Ar (%)	^{40}Ar/^{39}Ar	Apparent age (Ma)[d]	Exposure age (Ma)[e]
Bulk Rock	mass = 0.00349 g											
0.31 W	13.80 ± 0.30	1246 ± 576	23.5 ± 5.4	11.0 ± 15.0	3351 ± 12	33 ± 26	11.07 ± 15.17	2313 ± 1070	1.3	305.76 ± 418.70	5853 ± 2375	314.2 ± 547.1
0.88 W	18.67 ± 0.33	8021 ± 445	53.7 ± 4.7	27.4 ± 11.6	3684 ± 12	76 ± 58	27.69 ± 11.75	14890 ± 902	4.4	134.44 ± 56.98	4459 ± 701	117.3 ± 76.4
1.40 W	23.68 ± 0.61	15066 ± 391	34.2 ± 3.9	31.9 ± 10.2	3224 ± 22	49 ± 37	32.26 ± 10.31	27969 ± 991	8.1	101.00 ± 32.19	3993 ± 514	37.0 ± 37.2
2.28 W	38.79 ± 0.50	39209 ± 205	52.3 ± 4.2	40.1 ± 5.2	3205 ± 28	74 ± 56	40.55 ± 5.37	72786 ± 1800	12.7	79.86 ± 10.42	3621 ± 207	21.5 ± 14.7
2.80 W	44.94 ± 0.52	53421 ± 458	67.7 ± 2.4	29.1 ± 11.8	3416 ± 12	96 ± 73	29.38 ± 11.98	99170 ± 2544	16.1	117.48 ± 47.81	4238 ± 665	20.8 ± 8.2
3.52 W	86.55 ± 0.49	107651 ± 472	130.8 ± 4.4	48.1 ± 11.9	6505 ± 16	186 ± 140	48.59 ± 12.04	199842 ± 4911	21.6	135.28 ± 33.35	4469 ± 409	19.9 ± 5.5
4.25 W	150.47 ± 0.72	193582 ± 410	229.4 ± 3.2	71.2 ± 8.8	9203 ± 20	326 ± 246	71.92 ± 9.06	359361 ± 8722	29.8	129.30 ± 16.00	4395 ± 208	19.5 ± 2.6
4.97 W	444.20 ± 1.29	594365 ± 1041	684.5 ± 4.6	103.9 ± 20.9	14736 ± 19	972 ± 734	104.98 ± 21.24	1103366 ± 26747	41.6	141.84 ± 28.49	4548 ± 336	19.0 ± 1.1
5.49 W	518.94 ± 1.45	703757 ± 1335	810.8 ± 2.5	96.6 ± 28.1	14822 ± 22	1151 ± 870	97.62 ± 28.51	1306440 ± 31684	52.6	153.42 ± 44.65	4678 ± 488	19.0 ± 0.8
5.65 W	365.27 ± 1.05	496627 ± 960	567.3 ± 3.9	64.6 ± 20.4	10730 ± 17	806 ± 609	65.29 ± 20.68	921928 ± 22361	59.9	166.07 ± 52.46	4811 ± 532	18.8 ± 1.2
5.91 W	542.58 ± 1.45	741048 ± 1474	843.8 ± 3.2	120.6 ± 31.8	18662 ± 30	1198 ± 905	121.91 ± 32.24	1375666 ± 33373	73.6	154.68 ± 40.74	4692 ± 442	18.8 ± 0.8
6.27 W	243.12 ± 0.67	334329 ± 724	384.6 ± 4.8	80.4 ± 16.2	11536 ± 18	546 ± 413	81.24 ± 16.45	620641 ± 15066	82.8	143.48 ± 28.85	4567 ± 336	19.0 ± 1.9
6.79 W	98.74 ± 0.55	133252 ± 778	148.9 ± 5.1	39.7 ± 19.9	5744 ± 17	211 ± 160	40.15 ± 20.14	247365 ± 6153	87.3	144.59 ± 72.45	4579 ± 834	18.3 ± 4.8
7.49 W	99.81 ± 0.73	135553 ± 768	148.2 ± 3.8	46.3 ± 19.6	6648 ± 16	211 ± 159	46.80 ± 19.86	251638 ± 6249	92.6	143.54 ± 60.81	4567 ± 705	17.9 ± 4.1
8.19 W	111.10 ± 0.70	152743 ± 572	165.7 ± 3.9	43.9 ± 14.3	6346 ± 17	235 ± 178	44.37 ± 14.44	283548 ± 6937	97.5	144.53 ± 46.91	4579 ± 541	17.8 ± 3.7
9.12 W	52.24 ± 0.52	70864 ± 435	78.2 ± 3.0	21.6 ± 11.1	3046 ± 8	111 ± 84	21.84 ± 11.28	131551 ± 3281	100	140.92 ± 72.70	4537 ± 857	18.1 ± 6.9
Total	2852.90 ± 6.59	3780735 ± 6170	4423.5 ± 32.2	876.5 ± 139.6	124858 ± 150	6282 ± 3371 ppm 63.81 ± 17.12	885.67 ± 141.58 ppm 9.92 ± 0.79	7018476 ± 123428 wt% 11.27 ± 0.10				
										Plateau age	4517 ± 290	18.9 ± 0.83
										Isochron age	4274 ± 320	
Bulk plagioclase	mass = 0.00227 g											
0.31 W	5.98 ± 0.23	1155 ± 253	18.0 ± 3.3	7.5 ± 6.6	999 ± 13	26 ± 20	7.62 ± 6.67	2144 ± 472	1	132.42 ± 115.82	4434 ± 1444	274.1 ± 445.1
1.35 W	31.17 ± 0.42	17561 ± 266	37.8 ± 2.7	36.2 ± 6.9	4427 ± 17	54 ± 41	36.60 ± 7.05	32599 ± 930	5.6	122.23 ± 23.36	4303 ± 316	34.2 ± 26.2
2.80 W	63.34 ± 0.67	72515 ± 383	91.5 ± 2.7	43.5 ± 9.7	4604 ± 21	130 ± 98	43.92 ± 9.85	134616 ± 3331	11.1	105.91 ± 23.61	4070 ± 362	20.6 ± 6.3
3.78 W	89.95 ± 0.67	116427 ± 463	139.2 ± 4.1	44.3 ± 11.4	5583 ± 21	198 ± 149	44.74 ± 11.61	216132 ± 5296	16.8	126.09 ± 32.59	4354 ± 426	19.7 ± 4.9
4.61 W	236.91 ± 0.86	314682 ± 755	362.9 ± 5.1	101.7 ± 16.7	13057 ± 27	515 ± 389	102.77 ± 17.06	584168 ± 14193	29.8	128.38 ± 21.08	4383 ± 273	19.0 ± 2.1
5.03 W	307.10 ± 1.23	419214 ± 834	476.9 ± 4.7	92.2 ± 16.7	12470 ± 29	677 ± 512	93.16 ± 17.05	778220 ± 18879	41.6	135.27 ± 24.55	4469 ± 303	18.8 ± 1.5
5.65 W	349.51 ± 1.37	475159 ± 954	533.8 ± 2.8	170.8 ± 19.2	23688 ± 50	758 ± 573	172.59 ± 19.88	882075 ± 21400	63.4	138.69 ± 15.63	4510 ± 191	18.5 ± 1.1
6.32 W	297.00 ± 1.11	405857 ± 1047	464.8 ± 6.0	148.0 ± 23.7	20459 ± 39	660 ± 499	149.53 ± 24.26	753423 ± 18319	82.3	138.26 ± 22.18	4505 ± 269	18.9 ± 1.8
6.94 W	134.94 ± 0.83	180710 ± 529	203.5 ± 4.2	65.7 ± 12.4	9261 ± 22	289 ± 218	66.37 ± 12.64	335466 ± 8170	90.6	141.01 ± 26.65	4538 ± 316	18.5 ± 3.2
7.87 W	81.61 ± 0.56	109906 ± 484	131.7 ± 3.4	40.2 ± 12.1	5795 ± 11	187 ± 141	40.58 ± 12.24	204027 ± 5014	95.8	144.29 ± 43.39	4576 ± 501	19.9 ± 4.7
8.81 W	65.09 ± 0.40	85953 ± 636	102.0 ± 4.6	33.1 ± 16.3	4594 ± 11	145 ± 110	33.43 ± 16.52	159561 ± 4034	100	138.85 ± 68.56	4512 ± 819	19.6 ± 7.0
Total	1662.61 ± 5.53	2199137 ± 4329	2562.3 ± 27.1	783.1 ± 97.5	104937 ± 174	3639 ± 2102 ppm 56.83 ± 8.2	791.33 ± 99.48 ppm 13.63 ± 0.43	4082431 ± 77455 wt% 10.08 ± 0.05				
										Plateau age		18.8 ± 0.88
Bulk pyroxene	mass = 0.0014 g											
0.31 W	2.60 ± 0.21	321 ± 259	3.1 ± 4.4	2.8 ± 6.8	602 ± 9	4 ± 7	2.88 ± 6.83	597 ± 482	2.6	211.68 ± 502.97	5221 ± 4050	150.4 ± 1859.7
2.33 W	9.86 ± 0.18	9362 ± 193	13.4 ± 4.3	21.6 ± 5.0	1668 ± 11	19 ± 16	21.81 ± 5.12	17379 ± 553	22.1	77.28 ± 18.05	3570 ± 365	23.3 ± 63.3

Table 4. *Continued.* NWA 7325 ^{40}Ar-^{39}Ar analytical data calculated from each heating release step. Errors are given at the 2s level of uncertainty, n.d. = not determinable..

	Concentration (moles)											
Laser power (W)	^{36}Ar ($\times 10^{-18}$)	^{37}Ar ($\times 10^{-18}$)	^{38}Ar ($\times 10^{-18}$)	^{39}Ar ($\times 10^{-18}$)	^{40}Ar ($\times 10^{-18}$)	Cl ($\times 10^{-12}$)[a]	K ($\times 10^{-12}$)[b]	Ca ($\times 10^{-12}$)[c]	Cum. ^{39}Ar (%)	^{40}Ar/^{39}Ar	Apparent age (Ma)[d]	Exposure age (Ma)[e]
4.25 W	32.57 ± 0.35	35564 ± 603	46.0 ± 4.5	26.0 ± 15.7	3084 ± 8	65 ± 50	26.25 ± 15.86	66020 ± 1949	45.6	118.71 ± 71.66	4255 ± 987	21.1 ± 17.0
5.60 W	1366.70 ± 3.00	1922488 ± 3349	2173.5 ± 4.4	58.9 ± 76.7	7407 ± 25	3087 ± 2332	59.56 ± 77.47	3568865 ± 86510	99.1	125.65 ± 163.40	4348 ± 2136	18.8 ± 0.5
6.89 W	164.23 ± 1.06	229326 ± 683	261.7 ± 3.8	1.0 ± 17.1 n.d.	152 ± 10	372 ± 281	1.04 ± 17.27 n.d.	425716 ± 10371	100.0 n.d.	147.81 ± 2451.85 n.d.	4616 ± 27616 n.d.	19.0 ± 2.5
8.76 W	93.45 ± 0.61	130829 ± 511	145.3 ± 5.2	110.4 ± 161.1	228 ± 9	206 ± 156	111.54 ± 162.78 ppm 3.12 ± 1.14	242867 ± 5948				18.4 ± 5.0
Total	1669.42 ± 6.54	2327889 ± 7046	2643.1 ± 21.8		13141 ± 66	3754 ± 4709 ppm 95.1 ± 29.8		4321444 ± 174715 wt% 17.31 ± 0.17		Plateau age	4481 ± 200	
										Isochron age	4368 ± 360	18.8 ± 0.99

[a]Determined from ^{37}Cl(n,γ,β)^{38}Ar: Cl = 9.0159 × 10^4.(^{38}Ar/β.J).(mole/mole); β = ((K/Cl).(^{38}Ar/^{39}Ar))$_{Hb3gr}$; (K/Cl)$_{Hb3gr}$ = 5.242; β = 0.7847 ± 0.0004.

[b]Determined from ^{39}K(n,p)^{39}Ar: K = (^{39}Ar/J).(K/^{40}K).(λ/λ$_e$).(mole/mole); λ/λ$_e$ = 9.54; K/^{40}K = 1.167 × 10^4; J = 0.08089 ± 0.00153 (including uncertainty on monitor ages).

[c]Determined from ^{40}Ca(n,a)^{38}Ar: Cl = 8.042 × 10^4.(^{37}Ar/a.J).(mole/mole); a = ((K/Ca).(^{37}Ar/^{39}Ar)$_{Hb3gr}$; (K/Ca)$_{Hb3gr}$ = 0.1674; *a* = 0.531 ± 0.001.

[d]Includes uncertainties on the *J* value.

[e]Calculated using the ratio of cosmogenic ^{38}Ar (from the relationship ^{38}Arc = (5.35 × ^{38}Ar-^{36}Ar)/(5.35–0.65): where 5.35 is the trapped ^{36}Ar/^{38}Ar solar wind ratio and 0.65 trapped ^{36}Ar/^{38}Ar cosmogenic ratio of Hennessy and Turner 1980) to the concentration of 37Ar (as a measure of sample CaO composition in the bulk rock [Irving et al. 2013], and minerals [this study]). 38Arc/37Ar ratios then provide apparent cosmic ray exposure (CRE) ages using the sample chemistry and 4π cosmogenic production of Eugster (1988).

Table 5. High precision trace element and Sr measurements of NWA 7325 compared CI chondrites.

	ppm Rb	ppm Sr	ppm Zr	ppm Nb	ppm Ta	ppm Nd	ppm Hf	ppm Lu	ppm Sm	ppm W	$^{87}Rb/^{86}Sr$	$^{147}Sm/^{144}Nd$	$^{176}Lu/^{177}Hf$	Zr/Hf	Nb/Ta	Ta/W	Hf/W	Zr/Nb
85 mg NWA 7325 split	0.125	169	0.173	0.0236	0.00146	0.0753	0.00653	0.00188	0.0220	0.00319	0.00214	0.1768	0.0409	26.5	16.2	0.46	2.05	7.3
± (2 s.d.)	0.0013	2	0.008	0.0009	0.00008	0.0008	0.00015	0.00004	0.0002	0.00006	0.00003	0.0004	0.0012	1.3	1.1	0.03	0.06	0.4
Abundance rel. to CI chondrite	0.054	22	0.048	0.083	0.097	0.16	0.061	0.075	0.14	0.033								
$^{87}Sr/^{86}Sr$																		0.699257
±2 SE																		14
$^{87}Sr/^{86}Sr$ (4.562 Ga)																		0.699114

CI chondrite abundances from Palme and O'Neill (2014).

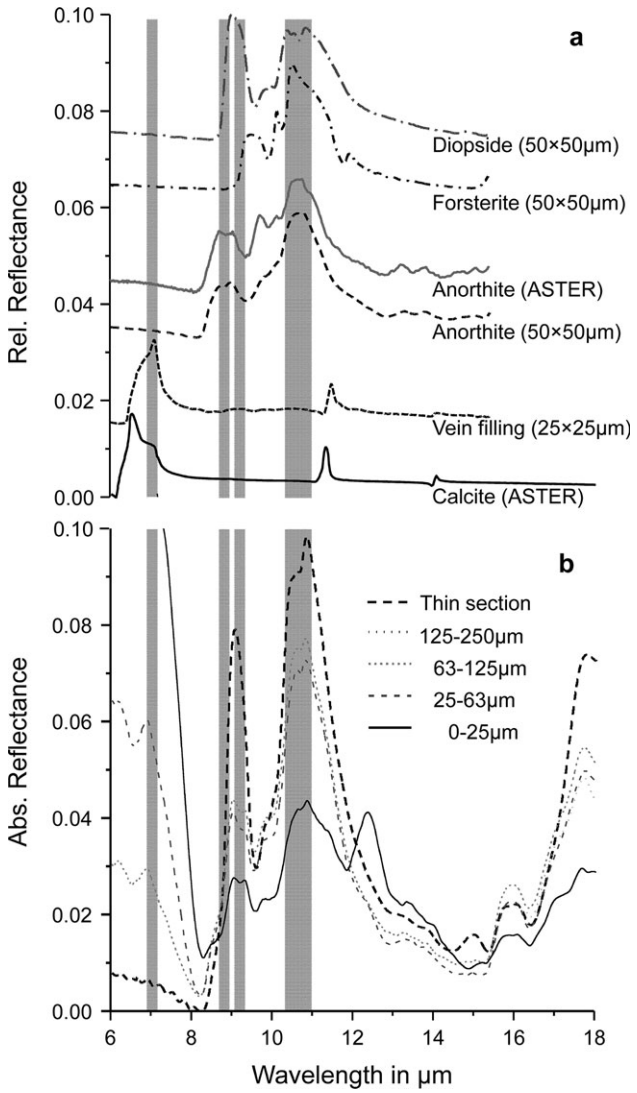

Fig. 6. a) FTIR microscope analyses of mineral phases of the polished thin section of NWA 7325 (in μm). Aperture sizes (and thus the analyzed area) were 50 × 50 μm for olivine, diopside, and anorthite, 25 × 25 μm for the filling of a vein. For comparison, reference spectra for anorthite and calcite are shown (Baldridge et al. 2009). The anorthite is similar except for a feature at 9.7 μm, which is lacking in the NWA 7325 data. However, the differences between the powder and thin section spectra could be also due to orientation effects of crystals in the thin section. The vein filling has its main features shifted compared to the reference, but the general similarity indicates a carbonatic composition of the veins. b) FTIR bulk spectra of dry-sieved powders from NWA 7325. The size fractions are 0–25, 25–63, 63–125, and 125–250 μm. While larger size fractions are similar, the fraction <25 μm exhibits a characteristic transparency feature at 12.3 μm. For comparison, a spectrum obtained from a 4 × 4 mm sized area on a thin section is shown as additional "bulk" spectrum. The spectrum is generally very similar to the larger size fractions, indicating a high degree of homogeneity at such small scale. Vertical gray bands in both figures mark the position of the characteristic features of the single mineral micro-FTIR spectra and reference data for the comparison with the bulk analyses.

symmetry. Furthermore, a pyroxene composition of Mg/(Mg+Fe+Ca) = 0.5 can be estimated following the approach of Wang et al. (2001).

Raman spectra of olivine (Fig. 7c) exhibit two main peaks as a double peak (DP), which are around 825 cm^{-1} and 857 cm^{-1}. This DP is associated with the internal stretching of the SiO_4 tetrahedron (ν_1 = symmetric stretching and ν_3 = asymmetric stretching) (Iishi 1978; Guyot et al. 1986; Price et al. 1987). In addition, the main peak positions of the forsterites are within the range of the forsterite (nearly Fo_{100}) contents determined by EPMA compared with investigations made by Kuebler et al. (2006), who extracted various olivine compositions from Raman spectral peak positions.

Furthermore, a relationship exists between the Raman spectral pattern of the main peaks and the crystallographic orientation of forsterites, based on the relative intensities of DP lines. Ishibashi et al. (2008) investigated Raman spectra of a Fo_{89} olivine in the range of 700 cm^{-1} to 1050 cm^{-1}. This range includes the DP that is the most characteristic feature of olivine in Raman spectra. These authors found that the relative height of one of the DPs can be associated with the crystallographic orientation of the investigated olivine. The spectrum in Fig. 7c shows that this olivine is estimated to be orientated near the [100] axis. Lower Stokes lines show, if any, very slight effects on the change in orientation and cannot be used for identification.

Four minor phases could be analyzed by Raman microscopy. It is well known that sulfides are difficult to investigate with Raman because of possible laser-induced alteration and fluorescence (e.g., White 2009). Nevertheless, a sulfide (Fig. 8a) is identified with peaks at 220 cm^{-1}, 275 cm^{-1}, and 480 cm^{-1} (Downs 2006; Avril et al. 2013). Magnesiochromite presents typical bands at 512 cm^{-1}, a shoulder peak at 654 cm^{-1}, and a main peak at 679 cm^{-1} (Fig. 8c; Downs 2006), which can be assigned to lattice vibrations (Lutz et al. 1991). Raman measurements of one bleb (compare also Fig. 5 lower image) within a sulfide identified it as magnetite that has a similar spectrum to magnesiochromite (compare Figs. 8c and 8d; Shebanova and Lazor 2003). Yong et al. (2012) and Wang et al. (2002) investigated the effect of pressure on $MgCr_2O_4$ at room temperature. According to their investigations, the magnesiochromite in NWA 7325 was not affected by a strong shock event that would have displaced the Stokes lines of the main peak to higher frequencies. Calcite is identified by a strong Raman band at 1090 cm^{-1} that is ascribed to the typical symmetric stretching vibration ν_1 (Gunasekaran et al. 2006). Another peak at 286 cm^{-1} belongs to the $CaCO_3$ translational lattice mode (Fig. 8b).

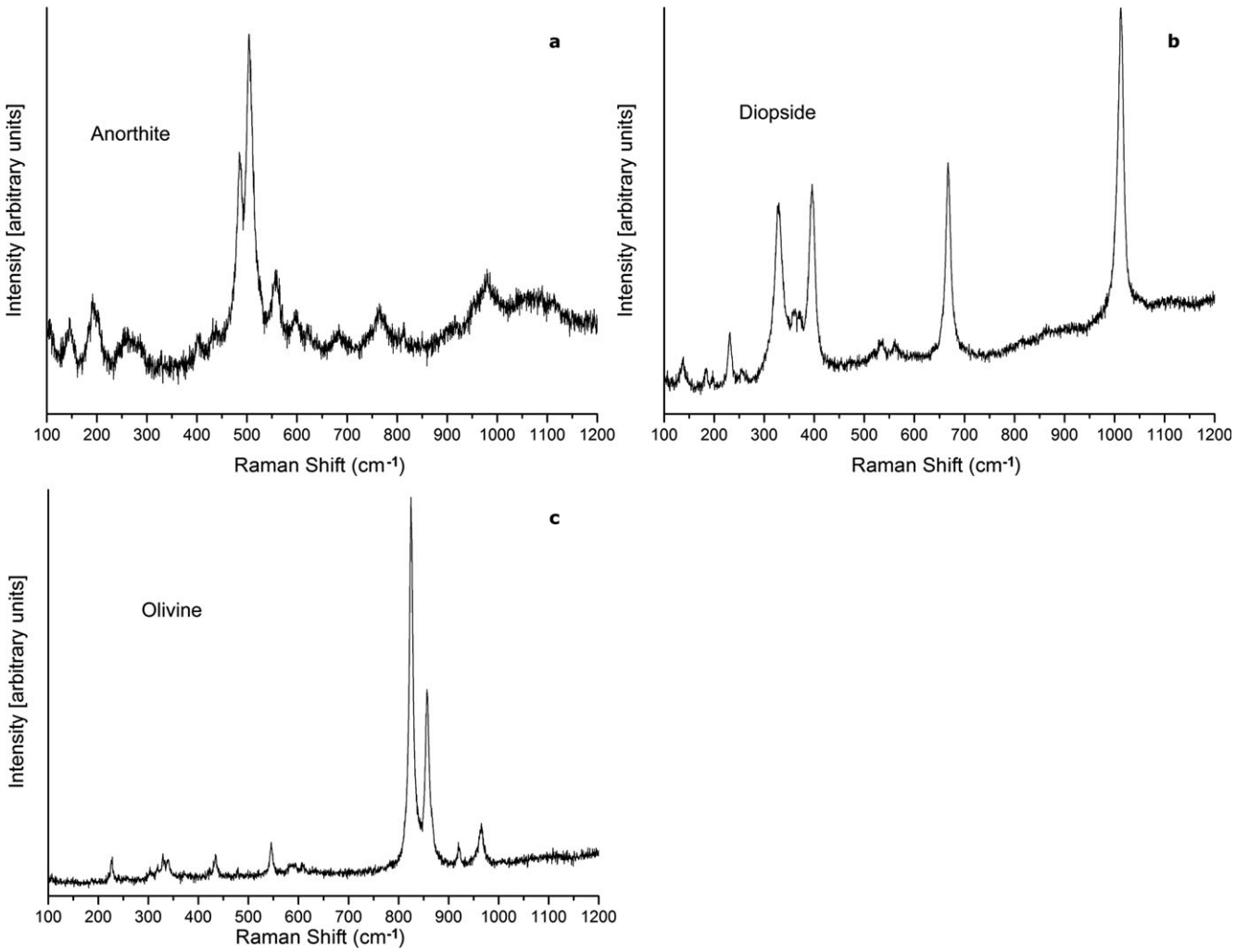

Fig. 7. Raman spectra at room temperatures of anorthite (a; main peaks: 486 cm^{-1}, 505 cm^{-1}), diopside (b; main peaks: 329 cm^{-1}, 395 cm^{-1}, 668 cm^{-1}, 1012 cm^{-1}), and olivine (c; main peaks: 825 cm^{-1}, 857 cm^{-1}) in NWA 7325 from 100 cm^{-1} to 1200 cm^{-1}.

Xenon and Argon Isotopic Composition

Isotopic ratios and ^{132}Xe concentrations measured in individual heating steps are given in Table 3. An elevated $^{129}Xe/^{132}Xe$ ratio is observed, with values up to ~1.47 in individual heating steps (Table 3; Fig. 9a). ^{129}Xe is produced by radioactive decay of ^{129}I (half-life 16 Ma), and excesses of ^{129}Xe can be chronologically significant in samples which closed to xenon loss when ^{129}I was still present. Hasegawa et al. (2014) reported a somewhat higher $^{129}Xe/^{132}Xe$ ratio of ~2.6 for a larger, 115 mg sample of NWA 7325.

Until a neutron-irradiated sample has been analyzed it is impossible to be definitive, but in our sample we observe that xenon released in midtemperature heating steps has a more or less constant $^{129}Xe/^{132}Xe$ ratio. This suggests either a trapped component with a signature inherited from a reservoir affected by ^{129}I decay or a host phase with iodine and xenon in reproducible proportions (Fig. 9b). The former would require processing after substantial decay of ^{129}I, several 10s of millions of years after solar system formation and thus resetting later than the reported $^{206}Pb/^{204}Pb$ age (Amelin et al. 2013). Higher temperature releases exhibit higher ratios (Fig. 9b). These higher ratios are possibly indicative of in situ decay of ^{129}I, as would be expected given from the early closure of the U-Pb system (Amelin et al. 2013).

The concentration of ^{132}Xe measured in this sample was $(4.03 \pm 0.02) \times 10^{-11}$ cm^3 STP g^{-1} (STP: standard temperature and pressure). The heavy isotopic composition is dominated by solar wind xenon mixing with fission xenon, Xe-Q, and/or terrestrial atmospheric contamination (Fig. 9c). However, there is no conclusive

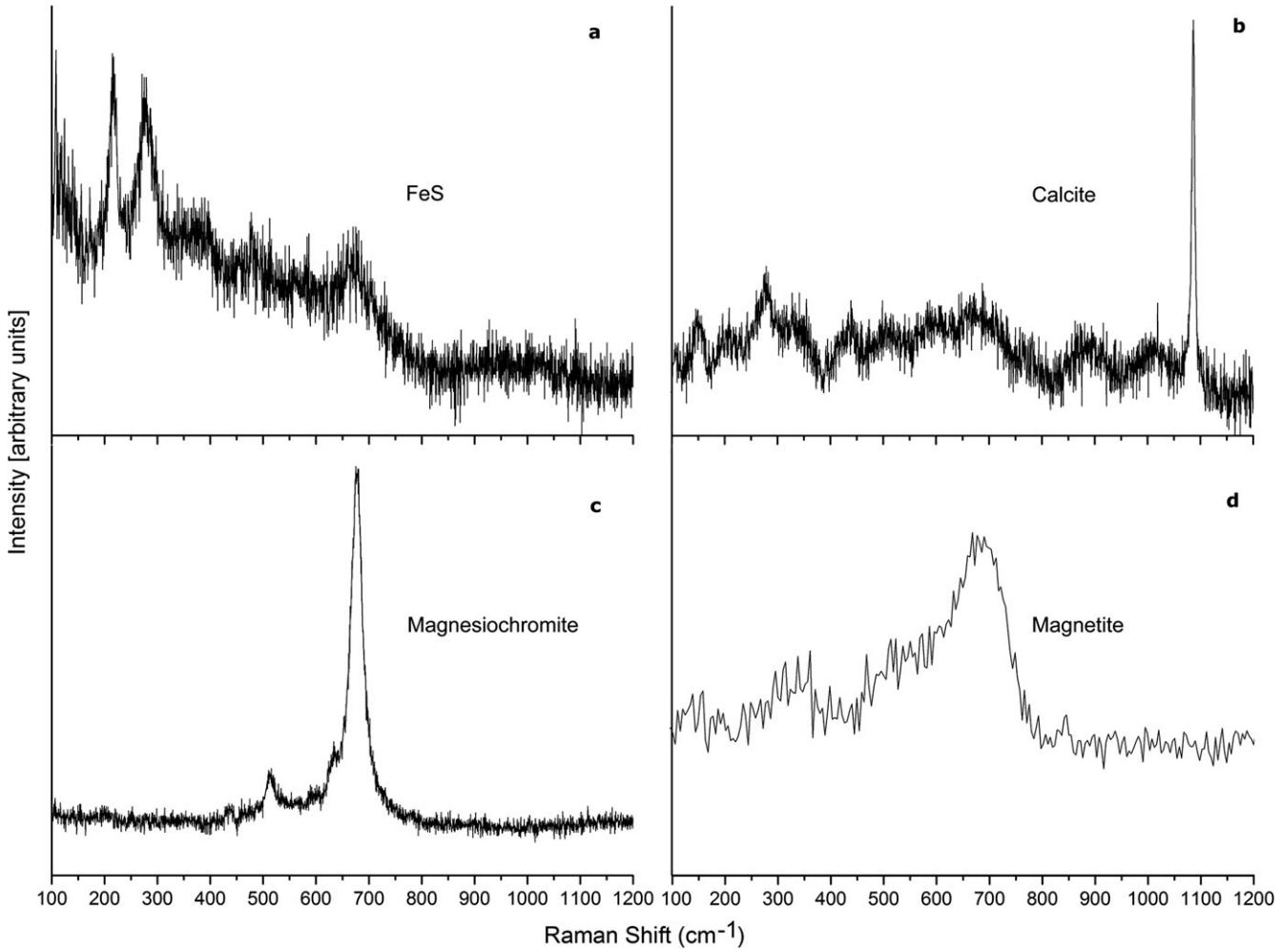

Fig. 8. Raman spectra at room temperatures of Fe-sulfide (a; main peaks: 220 cm^{-1}, 275 cm^{-1}), calcite (b; main peak: 1090 cm^{-1}), magnesiochromite (c; main peak: 679 cm^{-1}), and magnetite (d; main peak: 670 cm^{-1}) in NWA 7325 from 100 cm^{-1} to 1200 cm^{-1}.

evidence of fission xenon derived from ^{244}Pu or ^{238}U. There is also no evidence of a cosmogenic component. The absence of xenon isotopes derived from Pu, U, and the large ion lithophiles that are targets for xenon production by cosmic ray spallation (Ba, LREE) is consistent with the low abundance of these elements previously reported (Irving et al. 2013).

Argon isotope concentrations and derived chemistry measured in individual heating steps are given in Table 4. During stepped heating, the low-temperature steps show initial relatively high $^{40}Ar/^{39}Ar$ values, possibly related to the release of atmospheric ^{40}Ar hosted in terrestrial alteration products and evidenced by $^{40}Ar/^{36}Ar$ ratios of ~240 approaching modern air ($^{40}Ar/^{36}Ar_{air} \sim 298.56$). These temperature steps in the bulk sample and pyroxene split also have high (>1.7) $^{38}Ar/^{36}Ar$ values, consistent with the presence of some Cl-derived $^{38}Ar_{Cl}$, which could also have been released from terrestrial alteration products (such as the carbonate minerals identified in veining: see the FTIR Spectra section).

Most other extractions give $^{38}Ar/^{36}Ar$ ratios of ~1.5 consistent with being dominated by a cosmogenic ^{36}Ar component rather than solar. Thus, there is essentially no trapped solar wind implanted signature in the sample, consistent with the parent rock being buried at depth below surface regolith levels and no other trapped ^{40}Ar components. This is also borne out from examining the $^{39}Ar/^{40}Ar$ versus $^{36}Ar/^{40}Ar$ ratios in the three sample splits using an inverse isochron plot. These are displayed in Fig. 10 where all of the $^{36}Ar/^{40}Ar$ data sit close to the radiogenic intercept. From isochron the $^{40}Ar/^{36}Ar$ intercept of the bulk sample is 6.7 ± 6.9 and plagioclase is 3 ± 13 (Fig. 10). Correcting the data for this range of $^{40}Ar/^{36}Ar$ trapped values makes essentially no difference in the apparent ages and assuming that

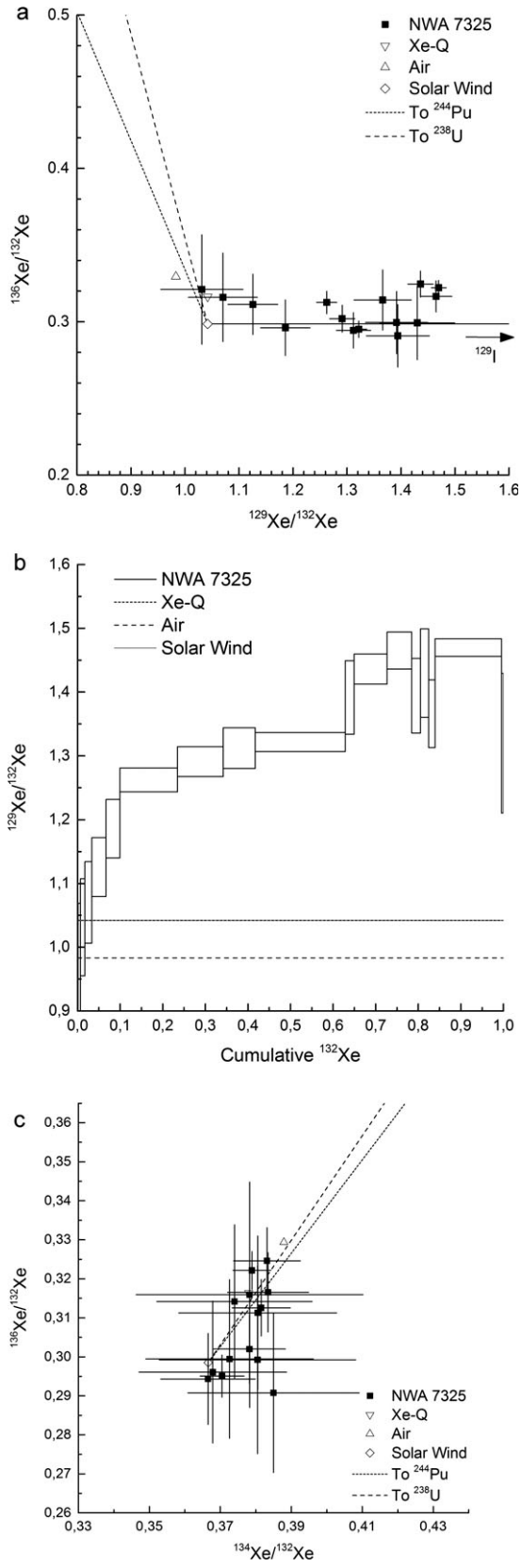

Fig 9. Data from xenon isotopic analysis of a single, 1.67 mg sample of NWA 7325. a) Individual heating steps show excesses of ^{129}Xe from decay of ^{129}I, with maximum ^{129}Xe/^{132}Xe ratios of ~1.47. Data that released less than 10,000 atoms of ^{132}Xe (<5 × blank) are not plotted. b) ^{129}Xe/^{132}Xe ratios measured in individual heating steps, plotted as a function of the cumulative total of ^{129}Xe. Xenon released in midtemperature heating steps has a more or less constant ^{129}Xe/^{132}Xe ratio suggesting an evolved trapped component. Higher temperature heating steps exhibit higher ^{129}Xe/^{132}Xe ratios, possibly indicative of in situ decay of ^{129}I. c) The composition of the heavy isotopes is dominated by solar wind xenon mixing with fission xenon, Xe-Q, and/or terrestrial atmospheric contamination, although there is no conclusive evidence for xenon derived from fission of ^{244}Pu or ^{238}U. Data that released less than 10,000 atoms of 132Xe (<5× blank) are not plotted.

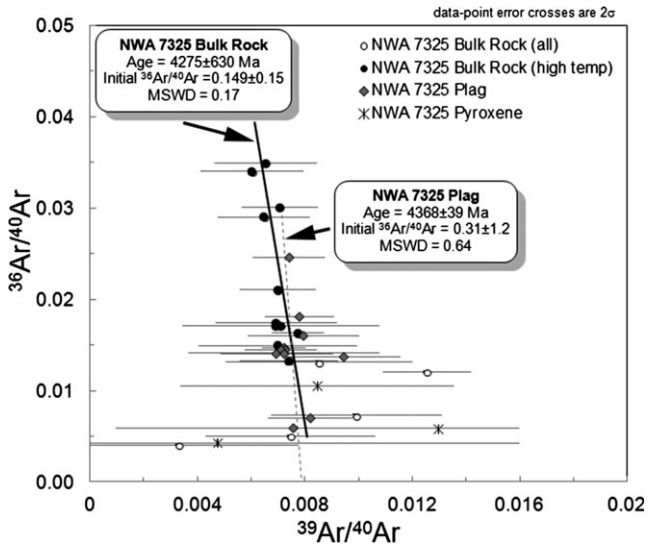

Fig. 10. Inverse argon isotope isochron of ^{39}Ar/^{40}Ar versus ^{36}Ar/^{40}Ar ratios for NWA 7325 bulk sample, plagioclase and pyroxene subsplits (data in Table 4). Solid black line is a fit to bulk sample high temp steps (closed circle symbols), and dashed gray line is a fit to the plagioclase mineral separate steps (gray diamonds) giving model isochron ages and initial ^{40}Ar/^{36}Ar ratios of 6.7 ± 6.9 (2σ) for the bulk sample and 3 ± 13 (2σ) for the plagioclase separate.

any small amounts of trapped noble gases have an initial ^{40}Ar/^{36}Ar ratio of 0, model age spectra are shown in Fig. 11.

The bulk sample has a plateau release ^{40}Ar/^{39}Ar age from 87.3% of the ^{39}Ar released of 4516 ± 160 Ma (2σ) (Fig. 11a), a minimum step age (at 12.7% of the ^{39}Ar gas release) of 3621 ± 204 Ma, and an exposure plateau age of 18.89 ± 0.83 Ma (Fig. 12a). The K/Ca plot was slightly curved with low temp release of K-rich terrestrial contamination (>0.001 K/Ca), although is essentially flat at higher temp steps with K/Ca ratio of 0.0001–0.0002 (Fig. 11a).

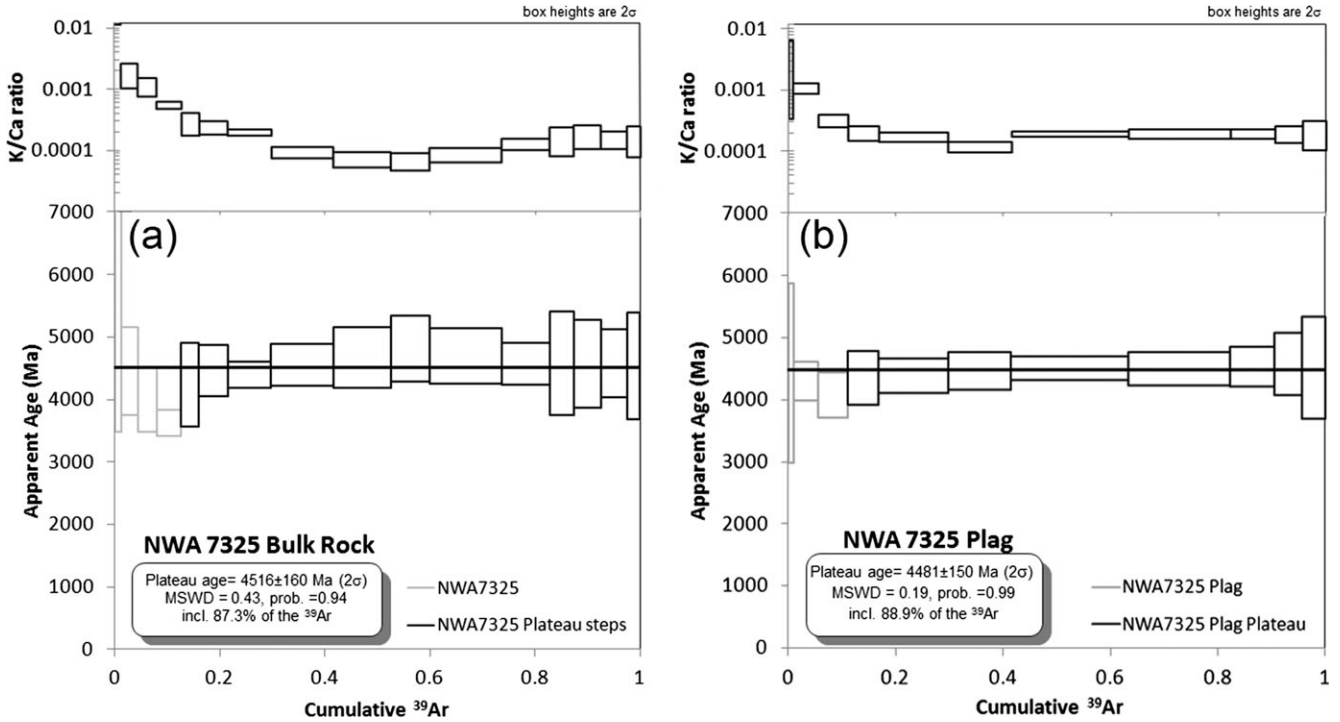

Fig. 11. Results of apparent ages calculated from Ar-Ar stepped heating of a bulk sample (a) and a plagioclase mineral separate (b). Top panels show K/Ca moles values derived from $^{39}Ar/^{37}Ar$ ratio released at each temperature step versus cumulative % of ^{39}Ar released from each step-heating. These are compared in the lower panels with the apparent ^{40}Ar-^{39}Ar age spectra where each box represents a single step release including a 2σ error. The black horizontal line across the age spectra plots defines the calculated plateau age. Those release steps that define a plateau are shown as a black box, and those (low-temperature releases) that did not contribute to the age plateau are outlined in gray.

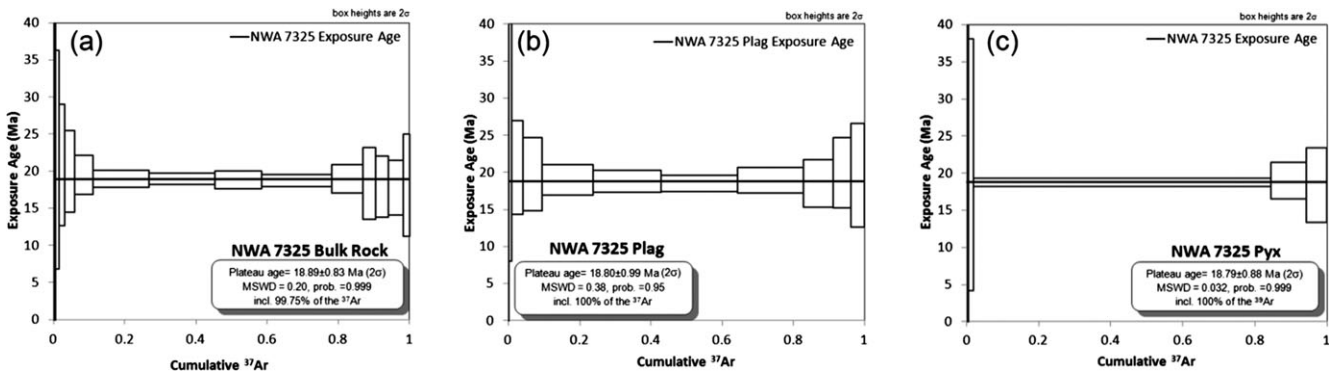

Fig. 12. Results of exposure ages calculated from Ar-Ar stepped heating of a bulk sample (a), a plagioclase mineral separate (b), and a pyroxene mineral separate (c). The black horizontal line across the age spectra plots defines the calculated plateau age.

The plagioclase separate has a plateau release $^{40}Ar/^{39}Ar$ age from 88.9% of the ^{39}Ar released of 4481 ± 150 Ma (2σ) (Fig. 11b) and an exposure plateau age of 18.80 ± 0.99 Ma (Fig. 12b). The K/Ca plot was slightly curved with low temp release of K-rich terrestrial contamination (>0.001 K/Ca), although it is flat at higher temp steps with K/Ca ratio of 0.0002 (Fig. 11b).

The pyroxene separate has such low K-content and high Ca-content that $^{40}Ar/^{39}Ar$ age errors are very large (Table 4); however, the sample records a minimal degassing age (at 22.1% of the ^{39}Ar gas) of 3570 ± 363 Ma (Table 4). The pyroxene subsplit gives a reliable exposure plateau age of 18.79 ± 0.88 Ma (Fig. 12c).

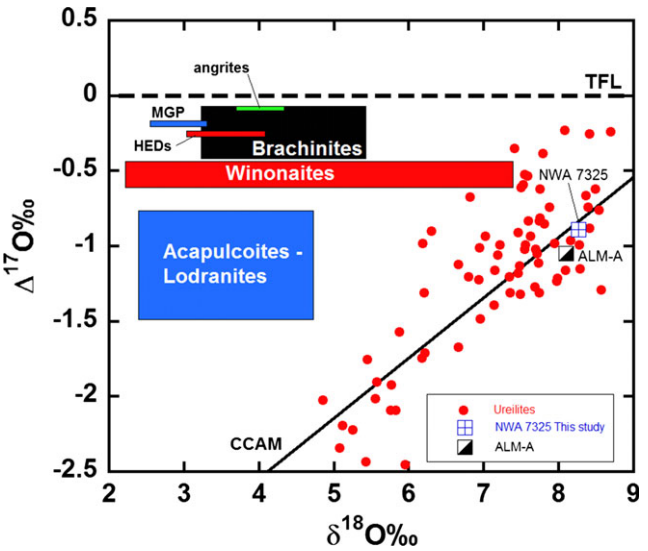

Fig. 13. Oxygen isotope composition of NWA 7325 shown in relation to the ureilite analyses of Clayton and Mayeda (1996) and Downes et al. (2008) and the compositional fields for primitive and differentiated achondrites defined by Greenwood et al. (2012). Data for the trachyandesitic fragment ALM-A from the Almahata Sitta meteorite from Bischoff et al. (2014). TFL = terrestrial fractionation line, CCAM = carbonaceous chondrite anhydrous mineral line (Clayton and Mayeda 1999), MGP = main group pallasites, HEDs = howardite eucrite diogenite clan.

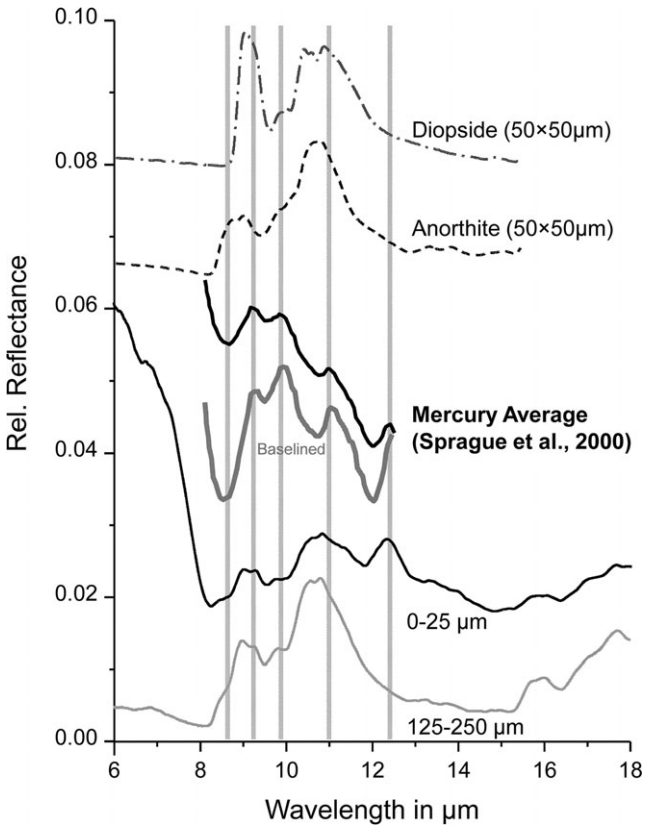

Fig. 14. Comparison of FTIR bulk powder spectra (0–25 μm, 125–250 μm), and anorthite and diopside Micro-FTIR spectra to an astronomical infrared spectrum from Mercury (vertical gray bands) (Sprague et al. 2007). Although there are similarities to the base lined astronomical spectrum regarding the transparency feature of the 0–25 μm fraction (12.3 μm), and the strong feature at ~9 μm, most other features are significantly different.

Oxygen Isotope Results

Two replicate analyses of NWA 7325 gave the following combined results: $\delta^{17}O = 3.41 \pm 0.02‰$; $\delta^{18}O = 8.26 \pm 0.04‰$; $\Delta^{17}O = -0.89 \pm 0.00‰$. These analyses are essentially within error of the results reported by Irving et al. (2013). The oxygen isotope composition of NWA 7325 plots well outside the compositional fields for either differentiated (lunar samples, angrites, mesosiderites, HEDs) or primitive (winonaites, acapulcoites-lodranites, brachinites) achondrites and also well away from the field of main-group pallasites (Fig. 13) (Greenwood et al. 2012).

As noted by Irving et al. (2013), the oxygen isotope composition of NWA 7325 plots within the field defined by ureilites and close to the trachyandesitic fragment ALMA-A from the Almahata Sitta meteorite (Bischoff et al. 2014) (Fig. 13). The relationships, if any, among the ureilites, Almahata Sitta, and NWA 7325 are examined further in the discussion section below.

High Precision Trace Element and Sr Isotope Measurements

Our Nd, Sm, and Lu measurements (Table 5) broadly confirm the overall subchondritic REE abundances reported previously for NWA 7325 by Irving et al. (2013) but are somewhat lower (Nd = 0.16 m, Sm = 0.14, Lu = 0.075 × CI chondrite; Palme and O'Neill 2014). Importantly, our results obtained for HFSE (Table 5) are substantially lower than the values reported by Irving et al. (2013), with abundances ranging from 0.03 to 0.1 × CI chondritic. This is especially the case for the Hf concentration (6.53 ppb). The concentration obtained here is ~70× lower than the value given by Irving et al. (2013). Ratios involving entirely lithophile HFSEs like $^{176}Lu/^{177}Hf$ (0.0409) and Zr/Hf (26.5) are slightly depleted, compared with chondritic values (~0.034 and 34, respectively; Münker et al. 2003; Bouvier et al. 2008), as expected for olivine- and pyroxene-rich cumulates from undifferentiated achondrites. A lower than chondritic Zr/Nb ratio (7.3), however, is in marked contrast to this observation, because a much more elevated Zr/Nb of ~20 would be expected at such Lu/Hf and Zr/Hf ratios. Notably, the

Nb/Ta of NWA 7325 (16.2) lies below the value of ~20 that is found for most chondrites and oxidized achondrites (Münker et al. 2003, 2013). Values of Hf/W and Ta/W are only slightly elevated from the CI chondritic ratios (1.1 and 0.16, respectively; Palme and O'Neill 2014), in marked contrast to many achondrites and the silicate Earth that exhibit much more pronounced depletions of siderophile W. The Sm/Nd ratio of NWA 7325 ($^{147}Sm/^{144}Nd = 0.1786$) indicates a slight LREE enrichment compared to the CI chondritic value (0.1960, Bouvier et al. 2008), whereas $^{87}Rb/^{86}Sr$ is extremely low (0.00214 ± 3), similar to those reported for small differentiated asteroids (e.g., Hans et al. [2013] and references therein). The measured $^{87}Sr/^{86}Sr$ is 0.699257, and the age corrected value at 4.562 Ga (Amelin et al. 2013) is 0.6991114.

DISCUSSION

Implications from the Petrology and Mineralogy of NWA 7325

On the basis of the petrologic and mineralogical results presented above NWA 7325—with its combination of magnesium-rich silicates, feldspar with An up to ~94, and Cr-bearing sulfides—is clearly a unique sample that is unlike any other known achondrite. In contrast, the average composition of Ca-pyroxene ($En_{53}Wo_{46}$) is similar to clinopyroxenes found in acapulcoites and lodranites as well as Ca-pyroxenes in aubrites—which are rare in aubrites (Fig. 3). The anomalous superchondritic FeO/MnO ratio versus Mg# in olivine (Fig. 4) (Goodrich and Delaney 2000) is consistent with cumulate or extreme residue crystallization from an unusual Fe-poor magma, which was enriched in Mg and Ca.

NWA 7325 has an igneous origin (Irving et al. 2013; Goodrich et al. 2014a; Weber et al. 2014). However, there is also evidence (secondary plagioclase, crack fillings, SiO_2-normative melt, and remnants of twinning-like structures in plagioclase) indicative of a second short temperature rise probably during metamorphism followed by rapid cooling (e.g., Bischoff et al. 2013) or a remelting result of a heavy shock event (e.g., Irving et al. 2013). Our petrologic investigations support the theory of a secondary heating and melting event rather than an impact-related event, as the shock stage of the meteorite is only S2 according to the scheme of Stöffler et al. (1991) In addition, there is no significant low-temperature argon loss (Fig. 11), which should be the case after a complete melting following a heavy shock event. Furthermore, the occurrence of SiO_2-normative melts together with more sodic plagioclase, as found for example, within Ca-pyroxene, may indicate in situ formation of a late partial melt starting at grain boundaries and filling pre-existing fractures. Also remnants of twinning-like structures in plagioclase and the dissolution of pyroxene are suggestive of reheating. Remelting *or* secondary heating has also been noted for eucrites, probably triggered by a dike-like intrusion during metamorphism followed by rapid cooling (Yamaguchi et al. 2001; Roszjar et al. 2011).

FTIR Spectra

The mid-infrared reflectance spectra of size fractions and polished sections confirm the general petrological observations of NWA 7325. The high similarity of the averaged olivine and pyroxene micro-IR spectra to the reference data indicates a low degree of crystal orientation. However, the lack of a significant feature in anorthites at 9.7 μm could be due to preferred orientation of this phase. The spectra of the carbonate veins infilling fracture networks suggest that this meteorite has undergone terrestrial alteration.

The anorthite IR spectra can also be used to estimate shock pressures during impact metamorphism. With increasing shock pressure, the feature at 9 μm weakens, disappearing at pressures higher than ~16 GPa (Johnson 2012). As this band is clearly visible in all the single anorthite spectra used for averaging, the material most likely suffered only weak impact shock (French 1998).

Raman

The Raman spectra of the polished thin section are also consistent with the general petrology of NWA 7325. The same composition is derived from olivine and pyroxene spectra as from the EMPA. In addition, there is no evidence for a heavy shock event in anorthite. Plagioclase is susceptible to shock events, which are exhibited by the loss of significant Raman bands resulting in smoothed spectra (Fritz et al. 2005). Raman spectra of anorthite with band broadening and a slight increase in the background indicate only a weak shock event (Fritz et al. 2005). Furthermore, our results demonstrate the presence of a low-temperature anorthite, with its stability field at low temperatures. In addition, in spectra of magnesiochromite the Raman peak positions are not shifted. Such a shift is expected after a shock event, because if magnesiochromite is exposed to strong shock waves, it undergoes a phase transition. This transition results in a displacement of the Stokes lines (Wang et al. 2002), which does not transform back after decompression (Yong et al. 2012). Thus, the observed peak positions of magnesiochromite also exclude a heavy shock event. In addition, we identified calcite, which most probably resulted from terrestrial weathering. This confirms the IR results, which detected calcium carbonate veins.

Xenon and Argon Isotopic Compositions

Our data indicate a component with a consistent $^{129}Xe/^{132}Xe$ ratio released up to intermediate temperatures; a component with a higher ratio is indicated by our highest temperature steps and the data of Hasegawa et al. (2014). A consistent, elevated $^{129}Xe/^{132}Xe$ ratio requires formation of a xenon reservoir that sampled a high I/Xe environment after substantial ^{129}I decay. If this component was incorporated at the time of crystallization, the $^{127}I/^{132}Xe$ ratio of the reservoir must have been in the region of 20000; if it was introduced into the rock after the complete decay of ^{129}I by later processing, a lower $^{127}I/^{132}Xe$ ratio of around 4000 is implied. The intermediate temperature data thus suggest a resetting event consistent with the second heating event several 10s of millions of years after solar system formation. In addition, a thermal event is at first glance consistent with the Ar/Ar thermochronology (Weiss et al. 2014). These authors report a major thermal event at 500 Ma, but there is no further evidence for external fluids. It is possible that this reheating event allowed indigenous xenon to mix with radiogenic xenon from ^{129}I decay in a closed environment to produce a mixed component that was then retrapped. However, the data with higher $^{129}Xe/^{132}Xe$ ratios suggest that at least some minerals with high blocking temperatures have recorded the signature of in situ ^{129}I decay. Overall, this sample provides further opportunities to test the proposed cross-calibration of the I-Xe and Pb-Pb systems (Gilmour et al. 2009) and to understand the behavior of iodine and xenon in the first basalts that contributed to the ultimate xenon isotopic signature of terrestrial planet volatile reservoirs.

There is good agreement between the Ar-Ar plateau ages recorded by the plagioclase and bulk sample subsplit. The individual step releases or plateau ages (Fig. 11, Table 4) do not record any degassing events during the last 3.6 Ga. These ages differ from those initially reported by Weiss et al. (2014), who suggest a resetting even occurred as recently as ~500 Ma. It is unclear if the ~4.5 Ga plateau ancient ages represent the original magmatic crystallization age, or a later thermal reheating event as suggested by the petrology results of this study; however, these are in good agreement with the 4562.5 ± 4.4 Ma early solar system event recorded by the U-Pb isotope system (Amelin et al. 2013). The cosmogenic exposure ages recorded by all three samples are internally consistent with an exposure age of 18.8–18.9 Ma and match well the exposure age of ~20 Ma reported by Hasegawa et al. (2014), who investigated noble gases.

Oxygen Isotope Composition of NWA 7325

On the basis of its oxygen isotope composition, NWA 7325 is unrelated to any of the major groups of primitive or differentiated achondrites, with the possible exception of the ureilites and the trachyandesitic fragment ALMA-A from the Almahata Sitta polymict breccia (Fig. 13). A further point of similarity between the ureilite meteorites and NWA 7325 is the high Ca and Cr content of olivine in both groups (Mittlefehldt et al. 1998) (Table 2), although Cr values in NWA 7325 are somewhat below the range seen in ureilites (Mittlefehldt et al. 1998). However, despite the fact that the oxygen isotope analysis of NWA 7325 plots within the ureilite field, a relationship with this group seems unlikely on the basis of their distinct chromium isotopic compositions (Sanborn et al. 2013). Oxygen isotope analyses indicate that NWA 7325 represents a unique achondrite from a parent body that is otherwise absent in the current meteorite record.

High Precision Trace Element and Sr Isotope Measurements

The overall low, subchondritic abundances of HFSE and REE and the elevated Sr content of NWA 7325 determined by isotope dilution confirm a cumulate origin, where incompatible lithophile trace elements are typically depleted in the cumulates. However, the patterns found for HFSE ratios such as Nb/Ta, Hf/W, Ta/W, and Zr/Nb can shed new light on the redox conditions and possible metasomatic history during the petrogenesis of NWA 7325. The Nb/Ta ratio of NWA 7325 is clearly below the value reported for oxidized achondrites such as eucrites or angrites, but overlaps with low Nb/Ta values of more reduced achondrites (Münker et al. 2013). In accordance with the low Fe content and high Mg#, such low Nb/Ta indicate a moderately siderophile behavior of Nb at more reducing conditions. Alternatively, the low Nb/Ta may point toward refractory precursor materials such as CV chondrites with low Nb/Ta but this is inconsistent with the chromium isotope systematics. NWA 7325 has a $\varepsilon^{54}Cr$ value of -0.55 ± 0.08 (Sanborn et al. 2013), whereas the CV chondrites Mokoia and Allende have positive $\varepsilon^{54}Cr$ values of 3.46 ± 0.25 and 2.66 ± 0.39, respectively (Shukolyukov and Lugmair 2006). In contrast to the interferences from Nb/Ta, the low Hf/W and Ta/W are inconsistent with a highly reduced composition of NWA 7325. A much stronger depletion of W in the silicate fraction and much more elevated Ta/W and Hf/W would be expected for reduced compositions. Metasomatism by melts enriched in highly incompatible elements such as W, however, may provide a viable explanation for the low Hf/W, and such a model can also explain the Zr/Nb and Sm/Nd of NWA 7325 that are both lower than the chondritic value, indicating selective enrichment of highly

incompatible elements like Nb or LREE (cf. Irving et al. 2013). The extremely low Rb/Sr and initial $^{87}Sr/^{86}Sr$ ratio of NWA 7325 indicate an extreme volatile depletion of the precursor material, similar to many other achondrite groups (Hans et al. [2013] and references therein). Notably, the initial $^{87}Sr/^{86}Sr$ of NWA 7325 is slightly higher than initial values reported for angrites or eucrites that broadly have the same age. This feature can be accounted for by a slightly protracted history of volatile depletion in the precursor material of NWA 7325 compared to angrites and eucrites. Alternatively, the slightly elevated Sr isotope composition may be due to terrestrial weathering or alteration, as the analyzed split of NWA 7325 was not treated with acid prior to dissolution in order to avoid selective leaching of other trace elements being measured. Further studies of mineral separates are therefore required to fully evaluate these first Sr isotope results.

Relationship between NWA 7325 and Mercury

The low-iron content and the overall chemistry with high amounts of anorthite made NWA 7325 an excellent candidate to be the first meteorite from Mercury (Irving et al. 2013). Our study confirms that the meteorite does have these chemical and mineralogical similarities although we do not observe the presence of oldhamite in NWA 7325, which has been previously suggested to be a common mineral on the surface of Mercury (accounting for elevated surface sulfur abundances: e.g., Weider et al. 2012).

We caution that it is often difficult to compare the chemistry and mineralogy of meteorites that are not derived from the surface layers of a body (i.e., Joy et al. 2014; Calzada-Diaz et al. 2015) with remote sensing observations that only map the surface chemistry and mineralogy from the upper few microns down to a few meters (Nittler et al. 2011; Weider et al. 2012, 2014; Peplowski et al. 2015). As NWA 7325 was sourced from a parent body rock likely located below a planetary surface (e.g., buried primary crust or an intrusive igneous sample formed in depth), any comparison with Mercury mission or telescopic surface chemical or mineralogical data, collected from a wide spatial scale, should be viewed with caution.

As there was no IR instrument onboard the Messenger mission, there are only a few mid-infrared observations available for Mercury (Sprague et al. 1994, 2002, 2007; Emery et al. 1998; Sprague and Roush 1998; Cooper et al. 2001; Donaldson-Hanna et al. 2007). These are based on ground and airplane based telescopes, integrate surface areas from at least 10^4 to 10^6 km^2, and point toward a heterogeneous surface, dominated by plagioclase with minor pyroxene (Sprague et al. 2007).

This is, thus, an opportunity to use our laboratory data in a first (simplified) comparison with actual observations. It is also helpful in developing and optimizing techniques for the application of the laboratory data to the future remote sensing data from BepiColombo.

We compare our results with a selected astronomical infrared spectrum from Mercury (Fig. 14), obtained by Mid-Infrared Array Camera (MIRAC) at the Kitt Peak Observatory. The spectrum is chosen due to its high signal to noise ratio and strong features, as well as complete spectral coverage in the region of interest for MERTIS, 7–14 μm. The observed region is very large and is the average of several observations and covers an area centered on ~210 to 250° longitude (Sprague et al. 2000). The emissivity data are recalculated from emissivity to reflectance using Kirchoff's law (e.g., Hapke 1993). Although the baselined spectrum shows a CF like feature at 8.5 μm, it is clearly different from the range of CF positions measured in the laboratory for NWA 7325 (8.1–8.3 μm). The Mercury spectrum exhibits strong RB at 9.3 μm, overlapping with the "double" feature in the NWA 7325 spectrum at 9–9.3 μm. An additional feature in the Mercury spectrum at 11.0 μm is close to the features at 10.6–10.8 μm in the meteorite; however, there is no overlap. The strongest feature in the astronomical spectrum is at 9.9 μm, while the meteorite spectrum shows a shoulder at 9.8 μm (Fig. 14). A potential transparency band in the Mercury spectrum located at 12.4 μm is very close to the transparency-like feature (TF) in the meteorite at 12.3 μm. TFs in the 12.0–12.7 μm region are also observed in various other spectra of Mercury (Cooper et al. 2001; Sprague et al. 2007). Additionally, these ground-based spectral observations of Mercury (Sprague et al. 2000) conclude that the best fit is terrestrial sodalite (a Na-rich feldspathoid), whereas we only observe an anorthitic plagioclase in NWA 7325.

Therefore, although there are certain similarities between the spectra, they are clearly not sufficient to constrain if the meteorite is a sample from Mercury based on the mid-infrared data.

SUMMARY AND CONCLUSIONS

On the basis of our comprehensive investigations, we conclude that NWA 7325 is an igneous cumulate rock from a unique achondrite parent body that experienced fast cooling after a second (partial) melting event. NWA 7325 is unlikely to originate from Mercury, in particular because it is extremely volatile

depleted and it seems to be much too old to originate from this planet. Furthermore, the Cr-content, as well as the Al/Si ratio of 0.45, does not fit with the composition expected for a sample from Mercury. High precision W and REE measurements point toward a metasomatic overprint of the cumulate by a later melting event. Investigations of the xenon and argon isotopes are also consistent with a second heating event resetting the system. However, the argon isotope data record ancient plateau ages that have not been reset. No evidence for high shock pressure can be found, because an intense shock heating is not recorded. Petrological, cosmochemical, infrared, and Raman investigations indicate that the sample originated from a previously unknown lithology on a highly reduced, iron-poor parent body or from a differentiated body that underwent large scale metal-silicate fractionation at reducing conditions. While both the oxygen isotope and olivine composition of NWA 7325 point to geochemical similarities with the ALMA-A trachyandesitic fragment of the Almahata Sitta polymict breccia and to ureilites (also compare Goodrich et al. 2014b), a single common source for these meteorites is unlikely.

Our study attests once more that IR is a powerful instrument to investigate mineral phases quickly and nondestructively, and therefore is an excellent tool for space missions—for distant observations as well as for orbital and rover missions. In addition, infrared spectroscopy is a technique that allows a direct link between meteorite samples and planetary bodies.

Acknowledgments—The authors thank U. Heitmann for sample preparation and H. Barden for her help in the FTIR microscope lab. D. Rothery, J. Fritz, and F. Jourdan as well as the AE G. Benedix have provided very helpful reviews, which greatly improved the manuscript. This work is supported by a Grant 50 QW 1302 from the Deutsches Zentrum für Luft- und Raumfahrt e.V. to H. Hiesinger in the framework of the BepiColombo mission. Some parts of the study are supported by the Leverhulme Grant 2011-569 and the Science and Technology Facilities Council (STFC) grant ST/J001643/1 and ST/L002957/1 at the University of Manchester. Oxygen isotope work at the Open University is supported by a consolidated grant from STFC.

Editorial Handling—Dr. T. Jull

REFERENCES

Amelin Y., Koefoed P., Iizuka T., and Irving A. J. 2013. U-Pb age of ungrouped achondrite NWA 7325 (abstract #5165). *Meteoritics & Planetary Science* 48.

Armstrong J. T. 1991. Quantitative elemental analysis of individual microparticles with electron beam instruments. In *Electron probe quantitation*, edited by Heinrich K. F. J. and Newbury D. E. New York: Plenum Press. pp. 261–315.

Avril C., Malavergne V., Caracas R., Zanda B., Reynard B., Charon E., Bobocioiu E., Brunet F., Borensztajn S., Pont S., Tarrida M., and Guyot F. 2013. Raman spectroscopic properties and Raman identification of CaS-MgS-MnS-FeS-Cr_2FeS_4 sulfides in meteorites and reduced sulfur-rich systems. *Meteoritics & Planetary Science* 48:1415–1426.

Baldridge A. M., Hook S. J., Grove C. I., and Rivera G. 2009. The ASTER Spectral Library Version 2.0. *Remote Sensing of Environment* 113:711–715.

Benedix G. K., Lauretta D. S., and McCoy T. J. 2005. Thermodynamic constraints on the formation conditions of winonaites and silicate-bearing IAB irons. *Geochimica et Cosmochimica Acta* 69:5123–5131.

Benkhoff J., vanCasteren J., Hayakawa H., Fujimoto M., Laakso H., Novara M., Ferri P., Middleton H. R., and Ziethe R. 2010. BepiColombo—Comprehensive exploration of Mercury: Mission overview and science goals. *Planetary and Space Science* 58:2–20.

Berlin J. 2009. Mineralogy and bulk chemistry of chondrules and matrix in petrologic Type 3 chondrites: Implications for early solar system processes. Ph.D. thesis, The University of New Mexico Albuquerque, New Mexico.

Bischoff A., Ward D., Weber I., Morlok A., Hiesinger H., and Helbert J. 2013. NWA 7325—Not a typical olivine gabbro, but a rock experienced fast cooling after a second (partial) melting event. European Planetary Science Congress, #427.

Bischoff A., Horstmann M., Barrat J.-A., Chaussidon M., Pack A., Herwartz D., Ward D., Vollmer C., and Decker S. 2014. Trachyandesitic volcanism in the early solar system. *Proceedings of the National Academy of Sciences* 111:12,689–12,692.

Bouvier A., Vervoort J. D., and Patchett P. J. 2008. The Lu–Hf and Sm–Nd isotopic composition of CHUR: Constraints from unequilibrated chondrites and implications for the bulk composition of terrestrial planets. *Earth and Planetary Science Letters* 273:48–57.

Brearley A. J. and Jones R. H. 1998. Chondritic meteorites. In *Planetary materials*, edited by Papike J. J. Reviews in Mineralogy, vol. 36. Washington, D.C.: Mineralogical Society of America. 400 p.

Burbine T. H., McCoy T. J., Nittler L. R., Benedix G. K., Cloutis E. A., and Dickinson T. L. 2002. Spectra of extremely reduced assemblages: Implications for Mercury. *Meteoritics & Planetary Science* 37:1233–1244.

Calzada-Diaz A., Joy K. H., Crawford I. A., and Nordheim T. A. 2015. Constraining the source regions of lunar meteorites using orbital geochemical data. *Meteoritics & Planetary Science* 50(2):214–228.

Clayton R. N. and Mayeda T. K. 1996. Oxygen isotope studies of achondrites. *Geochimica et Cosmochimica Acta* 60:1999–2017.

Clayton R. N. and Mayeda T. K. 1999. Oxygen isotope studies of carbonaceous chondrites. *Geochimica et Cosmochimica Acta* 63:2089–2017.

Cooper B., Potter A., Killen R., and Morgan T. 2001. Mid-infrared spectra of Mercury. *Journal of Geophysical Research* 106:32803–32814.

Corder C. A., Day J. M. D., Patchen A. P., Marti K., and Taylor L. A. 2013. Petrology of acapulcoites and

lodranites and the anomalous achondrite Lewis Cliff 88763 (abstract #2653). 44th Lunar and Planetary Science Conference. CD-ROM.

Crowther S. A., Mohapatra R. K., Turner G., Blagburn D. J., Kehm K., and Gilmour J. D. 2008. Characteristics and applications of RELAX, an ultrasensitive resonance ionization mass spectrometer for xenon. *Journal of Analytical Atomic Spectrometry* 23:921–1044.

Donaldson-Hanna K. L., Sprague A. L., Kozlowski R. W. H., Boccafolo K., and Warell J. 2007. Mercury and the Moon: Initial findings from mid-infrared spectroscopic measurements of the surface (abstract #2291). 38th Lunar and Planetary Science Conference. CD-ROM.

Downes H., Mittlefehldt D. W., Kita N. T., and Valley J. W. 2008. Evidence from polymict ureilite meteorites for a disrupted and re-accreted single ureilite parent asteroid gardened by several distinct impactors. *Geochimica et Cosmochimica Acta* 72:4825–4844.

Downs R. T. 2006. The RRUFF Project: An integrated study of the chemistry, crystallography, Raman and infrared spectroscopy of minerals. 19th General Meeting of the International Mineralogical Association, Kobe, Japan. O03-13.

Emery J. P., Sprague A. L., Witteborn F. C., Colwell J. E., Kozlowski R. W. H., and Wooden D. H. 1998. Mercury: Thermal modeling and mid-infrared (5–12 μm) observations. *Icarus* 136:104–123.

Eugster O. 1988. Cosmic-ray production rates for ^{3}He, ^{21}Ne, ^{38}Ar, ^{83}Kr, and ^{126}Xe in chondrites based on ^{81}Kr-Kr exposure ages. *Geochimica et Cosmochimica Acta* 52:1649–1662.

Freeman J. J., Wang A., Kuebler K. E., Jolliff B. L., and Haskin L. A. 2008. Characterization of natural feldspars by Raman spectroscopy for future planetary exploration. *Canadian Mineralogist* 46:1477–1500.

French B. M. 1998. Traces of catastrophe. A handbook of shock-metamorphic effects in terrestrial meteorite impact structures. LPI Contribution 954. Houston, Texas: Lunar and Planetary Institute. 120 p.

Fritz J., Greshake A., and Stöffler D. 2005. Micro-Raman spectroscopy of plagioclase and maskelynite in Martian meteorites: Evidence of progressive shock metamorphism. *Antarctic Meteorite Research* 18:96–116.

Gilmour J. D., Lyon I. C., Johnston W. A., and Turner G. 1994. RELAX: An ultrasensitive, resonance ionization mass spectrometer for xenon. *Review of Scientific Instruments* 65:617–625.

Gilmour J. D., Crowther S. A., Busfield A., Holland G., and Whitby J. A. 2009. An early I-Xe age for CB chondrite chondrule formation, and a re-evaluation of the closure age of Shallowater enstatite. *Meteoritics & Planetary Science* 44:573–579.

Goodrich C. A., and Delaney J. S. 2000. Fe/Mg—Fe/Mn relations of meteorites and primary heterogeneity of primitive achondrite parent bodies. *Geochimica et Cosmochimica Acta* 64:149–160.

Goodrich C. A., Kita N. T., and Nakashima D. 2014a. Petrology of the NWA 7325 ungrouped achondrite—Meteorite from Mercury, the ureilite parent body, or a previously unsampled asteroid (abstract #1246). 45th Lunar and Planetary Science Conference. CD-ROM.

Goodrich C. A., Harlow G. E., Van Orman J. A., Sutton S. R., Jercinovic M. J., and Mikouchi T. 2014b. Petrology of chromite in ureilites: Deconvolution of primary oxidation states and secondary reduction processes. *Geochimica et Cosmochimica Acta* 135:126–169.

Greenwood R. C., Franchi I. A., Gibson J. M., and Benedix G. K. 2012. Oxygen isotope variation in primitive achondrites: The influence of primordial, asteroidal and terrestrial processes. *Geochimica et Cosmochimica Acta* 94:146–163.

Gunasekaran S., Anbalagan G., and Pandi S. 2006. Raman and infrared spectra of carbonates of calcite structure. *Journal of Raman Spectroscopy* 37:892–899.

Guyot F., Boyer H., Madon M., Velde B., and Poirier J. P. 1986. Comparison of the Raman microprobe spectra of (Mg, Fe)2SiO4 and Mg2GeO4 with olivine and spinel structures. *Physics and Chemistry of Minerals* 13:91–95.

Hamilton V. E. 2000. Thermal infrared emission spectroscopy of the pyroxene mineral series. *Journal of Geophysical Research* 105:9701–9716.

Hamilton V. E. 2010. Thermal infrared (vibrational) spectroscopy of Mg–Fe olivines: A review and applications to determining the composition of planetary surfaces. *Chemie der Erde* 70:7–33.

Hans U., Kleine T., and Bourdon B. 2013. Rb–Sr chronology of volatile depletion in differentiated protoplanets: BABI, ADOR and ALL revisited. *Earth and Planetary Science Letters* 374:204–214.

Hapke B. 1993. Combined theory of reflectance and emittance spectroscopy. In *Remote geochemical analysis, elemental and mineralogical composition*., edited by Pieters C. M., and Englert P. A. J.. Cambridge: Cambridge University Press.

Hasegawa H., Haba M. K., Nagao K., Mikouchi T., and Bizzarro M. 2014. Noble gas and mineralogical studies of NWA 7325 ungrouped achondrite (abstract #5306). *Meteoritics & Planetary Science* 49.

Helbert J., Maturilli A., D'Amore M., Klima R. L., Izenberg N. R., Holsclaw G. M., and McClintock W. E. 2013. The Northwest Africa 7325 meteorite—A potential spectral analog for Mercury? European Planetary Science Congress #422.

Hennessy J. and Turner G. 1980. ^{40}Ar – ^{39}Ar ages and irradiation history of Luna 24. *Philosophical Transactions of the Royal Society London* A297:27–39.

Hiesinger H., Helbert J., and Co-I Team M. E. R. T. I. S. 2010. The Mercury Radiometer and Thermal Infrared Spectrometer (MERTIS) for the BepiColombo mission. *Planetary and Space Science* 58:144–165.

Horstmann M., and Bischoff A. 2014. The Almahata Sitta polymict breccia and the late accretion of asteroid 2008 TC_3. *Chemie der Erde—Geochemistry* 74:149–183.

Huang E., Chen C. H., Huang T., Lin E. H., and Xu J. 2000. Raman spectroscopic characteristics of Mg-Fe-Ca pyroxenes. *American Mineralogist* 85:473–479.

Iishi K. 1978. Lattice dynamics of forsterite. *American Mineralogist* 63:1198–1208.

Ikeda Y. and Takeda H. 1985. A model for the origin of basaltic achondrites based on the Yamato 7308 howardite. *Journal of Geophysical Research Solid Earth* 90:C649–C663.

Irving A. J., Kuehner S. M., Bunch T. E., Ziegler K., Chen G., Herd C. D. K., Conrey R. M., and Ralew S. 2013. Ungrouped mafic achondrite Northwest Africa 7325: A reduced, iron-poor cumulate olivine gabbro from a differentiated planetary parent body (abstract #2164). 44th Lunar and Planetary Science Conference. CD-ROM.

Ishibashi H., Arakawa M., Ohi S., Yamamoto J., Miyake A., and Kagi H. 2008. Relationship between Raman spectral pattern and crystallographic orientation of a rock-forming mineral: A case study of Fo89Fa11 olivine. *Journal of Raman Spectroscopy* 39:1653–1659.

Izenberg N. R., Klima R. L., Murchie S. L., Blewett D. T., Holsclaw G. M., McClintock W. E., Malaret E., Mauceri C., Vilas F., Sprague A. L., Helbert J., Domlingue D. L., Head J. W. III, Goudge T. A., Solomon S. C., Hibbitts C. A, and Dyar M. D. 2014. The low-iron reduced surface of Mercury as seen in spectral reflectance by MESSENGER. *Icarus* 228:364–374.

Jarosewich E., Nelen J. A., and Norberg J. A. 1980. Reference samples for electron microprobe analysis. *Geostandards Newsletters* 4:43–47.

Johnson J. R. 2012. Thermal infrared spectra of experimentally shocked andesine anorthosite. *Icarus* 221:359–364.

Joy K. H., Nemchin A., Grange M., Lapen T. J., Peslier A. H., Ross D. K., Zolensky M. E., and Kring D. A. 2014. Petrography, geochronology, and source terrain characteristics of lunar meteorites Dhofar 925, 961 and Sayh al Uhaymir 449. *Geochimica et Cosmochimica Acta*. 114:299–325.

Kirchenbaur M., Münker C., Schuth S., Garbe-Schönberg D., and Marchev P. 2012. Tectonomagmatic constraints on sources of eastern Mediterranean K-rich lavas. *Journal of Petrology* 53:27–65.

Kita N. T., Sanborn M. E., Yin Q.-Z., Nakashima D., and Goodrich C. A. 2014. The NWA 7325 ungrouped achondrite—Possible link to ureilites? Oxygen and chromium isotopes and trace element abundances (abstract #1455). 45th Lunar and Planetary Science Conference. CD-ROM.

Kuebler K., Jolliff B. L., Wang A., and Haskin L. A. 2006. Extracting olivine (Fo-Fa) composition from Raman spectral peak positions. *Geochimica et Cosmochimica Acta* 70:6201–6222.

Lee M. R., Smith C. L., Gordon S. H., and Hodson M. E. 2006. Laboratory simulation of terrestrial meteorite using the Besour (LL6) ordinary chrondrite. *Meteoritics & Planetary Science* 41:1123–1138.

Ludwig K. R. 2012. *User's manual Isoplot ?3.75. A geochronological toolkit for Microsoft Excel*. Berkeley, California: Berkeley Geochronology Center, Special Publication No. 5.

Lutz H. D., Müller B., and Steiner H. J. 1991. Lattice vibration spectra. LIX. Single crystal Infrared and Raman studies of spinel type oxides. *Journal of Solid State Chemistry* 90:54–60.

Marchi S., Chapman C. R., Fassett C. I., Head J. W., Bottke W. F., and Strom R. G. 2013. Global resurfacing of Mercury 4.0–4.1 billion years ago by heavy bombardment and volcanism. *Nature* 499:59–61.

McCoy T. J., Keil K., Clayton R. N., Mayeda T. K., Bogard D. D., Garrison D. H., Huss G. R., Hutcheon I. D., and Wieler R. 1996. A petrologic, chemical and isotopic study of Monument Draw and comparison with other acapulcoites: Evidence for formation by incipient partial melting. *Geochimica et Cosmochimica Acta* 60:2681–2708.

McCoy T. J., Keil K., Clayton R. N., Mayeda T. K., Bogard D. D., Garrison D. H., and Wieler R. 1997. A petrologic and isotopic study of lodranites: Evidence for early formation as partial melt residues from heterogeneous precursors. *Geochimica et Cosmochimica Acta* 61:623–637.

McKeown D. A. 2005. Raman spectroscopy and vibrational analyses of albite: From 25°C through the melting temperature. *American Mineralogist* 90:1506–1517.

McSween H. Y. Jr., Mittlefehldt D. W., Beck A. W., Mayne R. G., and McCoy T. J. 2011. HED meteorites and their relationship to the geology of Vesta and the Dawn Mission. *Space Science Reviews* 163:141–174.

Mernagh T. P. 1991. Use of the laser Raman microprobe for discrimination amongst feldspar minerals. *Journal of Raman Spectroscopy* 22:453–457.

Miller M. F., Franchi I. A., Sexton A. S., and Pillinger C. T. 1999. High precision $\delta^{17}O$ measurements of oxygen from silicates and other oxides: Method and applications. *Rapid Communications in Mass Spectrometry* 13:1211–1217.

Mittlefehldt D. W., McCoy T. J., Goodrich C. A., and Kracher A. 1998. Non- chondritic meteorites from asteroidal bodies. In *Planetary materials*, edited by Papike J. J. Reviews in Mineralogy, vol. 36. Washington, D.C.: Mineralogical Society of America. pp. 4–001-4-196.

Morlok A., Weber I., Ahmedi M., Bischoff A., Helbert J., and Hiesinger H. 2013. Ungrouped achondrite NWA 7325: Infrared and Raman study of a potential sample from Mercury. European Planetary Science Congress, #114.

Münker C. 2010. A high field strength element perspective on early lunar differentiation. *Geochimica et Cosmochimica Acta* 74:7340–7361.

Münker C., Weyer S., Scherer E., and Mezger K. 2001. Separation of high field strength elements (Nb, Ta, Zr, Hf) and Lu from rock samples for MC-ICPMS measurements. *Geochemistry, Geophysics, Geosystems (G3)*, 2:183–202. doi:10.1029/2001GC000183.

Münker C., Pfänder J. A., Weyer S., Büchl A., Kleine T., and Mezger K. 2003. Evolution of planetary cores and the Earth–Moon system from Nb/Ta systematics. *Science* 301:84–87.

Münker C, Fonseca R, and Schulz T. 2013. An extraterrestrial cause for the silicate Earth's Nb paradox? *Minalogical Magazine* 77:1809.

Nebel O., Mezger K., Scherer E. E., and Münker C. 2005. High precision determinations of $^{87}Rb/^{85}Rb$ in geologic materials by MC-ICP-MS. *International Journal of Mass Spectrometry* 246:10–18.

Nehru C. E., Zucker S. M., Harlow G. E., and Prinz M. 1980. Olivines and olivine coronas in mesosiderites. *Geochimica et Cosmochimica Acta* 44:1103–1118.

Nittler L. R., Starr R. D., Weider S. Z., McCoy T. J., Boynton W. V., Ebel D. S., Ernst C. M., Evans L. G., Goldsten J. O., Hamara D. K., Lawrence D. J., McNutt R. L. Jr., Schlemm C. E, Solomon S. C., and Sprague A. L. 2011. The major-element composition of Mercury's surface from MESSENGER X-ray spectrometry. *Science* 333:1847–1850.

Palme H., and O'Neill H. St. C. 2014. *Cosmochemical estimates of mantle composition*. Treatise on Geochemistry. Oxford: Elsevier. pp. 1–35.

Peplowski P. N., Lawrence D. J., Feldman W. C., Goldsten J. O., Bazell D., Evans L. G., Head J. W., Nittler L. R., Solomon S. C., and Weider S. Z. 2015. Geochemical terranes of Mercury's northern hemisphere as revealed by MESSENGER neutron measurements. *Icarus* 253:346–363.

Price G. D., Parker S. C., and Leslie M. 1987. The lattice dynamics of forsterite. *Mineralogical Magazine* 51:157–170.

Renne P. R., Mundil R., Balco G., Min K., and Ludwig K. R. 2010. Joint determination of ^{40}K decay constants and $^{40}Ar^*/^{40}K$ for the Fish Canyon sanidine standard, and improved accuracy for $^{40}Ar/^{39}Ar$ geochronology. *Geochimica et Cosmochimica Acta* 74:5349–5367.

Rocholl A., and Jochum K. P. 1993. Th, U and other trace elements in carbonaceous chondrites: Implications for the terrestrial and soar-system Th/U ratios. *Earth and Planetary Science Letters* 117:265–278.

Roszjar J., Metzler K., Bischoff A., Barrat J.-A., Geisler T., Greenwood R. C., Franchi I. A., and Klemme S. 2011. Thermal history of Northwest Africa (NWA) 5073—A coarse-grained Stannern-trend eucrite containing cm-sized pyroxenes and large zircon grains. *Meteoritics & Planetary Science* 46:1754–1773.

Rothery D. A., Marinangeli L., Anand M., Carpenter J., Christensen U., Crawford I. A., De Sanctis M. C., Epifani E. M., Erard S., Frigeri A., Fraser G., Hauber E., Helbert J., Hiesinger H., Joy K. H., Langevin Y., Massironi M., Milillo A., Mitrofanov I., Muinonen K., Näränen J., Pauselli C., Potts P., Warell J., and Wurz P. 2010. Mercury's surface and composition studied by BepiColombo. *Planetary and Space Science* 58:21–39.

Sanborn M. E., Yamakawa A., Yin Q.-Z., Irving A. J., and Amelin Y. 2013. Chromium isotopic studies of ungrouped achondrites NWA 7325, NWA 2976, and NWA 6704 (#5220). *Meteoritics & Planetary Science* 48.

Sarbadhikari A. B., Goodrich C. A., Liu Y., Day J. M. D., and Taylor L. A. 2011. Evidence for multiple enriched shergottite mantle sources in Mars from olivine-hosted melt inclusions in Larkman Nunatak 06319. *Geochimica et Cosmochimica Acta* 75:6803–6820.

Shebanova O. N. and Lazor P. 2003. Raman spectroscopic study of magnetite ($FeFe_2O_4$): A new assignment for the vibrational spectrum. *Journal of Solid State Chemistry* 174:424–430.

Shukolyukov A. and Lugmair G. W. 2006. Manganese chromium isotope systematic of carbonaceous chondrites. *Earth and Planetary Science Letters* 250:200–213.

Sprague A. L. and Roush T. L. 1998. Comparison of laboratory emission spectra with Mercury telescopic data. *Icarus* 133:174–183.

Sprague A. L., Kozlowski R. W. H., Witteborn F. C., Cruikshank D. P., and Wooden D. H. 1994. Mercury: Evidence for anorthosite and basalt from mid-infrared (7.5–13.5 micrometer) spectroscopy. *Icarus* 109:156–167.

Sprague A., Deutsch L. K., Hora J., Fazio G. G., Ludwig B., Emery J., and Hoffmann W. F. 2000. Mid-infrared (8.1–12.5 μm) imaging of Mercury. *Icarus* 147:421–432.

Sprague A. L., Emery J. P., Donaldson K. L., Russell R. W., Lynch D. K., and Mazuk A. L. 2002. Mercury: Mid-infrared (3–13.5 mm) observations show heterogeneous composition, presence of intermediate and basic soil types, and pyroxene. *Meteoritics & Planetary Science* 37:1255–1268.

Sprague A., Warell J., Cremonese G., Lengevin Y., Helbert J., Wurz P., Veselovsky I., Orsini S., and Milillo A. 2007. Mercury's surface composition and character as measured by ground-based observations. *Space Science Reviews* 132:399–431.

Stelzner T., Heide K., Bischoff A., Weber D., Scherer P., Schultz L., Happel M., Schrön W., Neupert U., Michel R., Clayton R. N., Mayeda T. K., Bonani G., Haidas I., Ivy-Ochs S., and Sutter M. 1999. An interdisciplinary study of weathering effects in ordinary chondrites from the Acfer region, Algeria. *Meteoritics & Planetary Science* 34:787–794.

Stephen N. R., Benedix G. K., Bland P. A., Hamilton V. E., Mariani E., and Prior D. J. 2010. Preferred orientation relationships of olivine and pyroxene in the Shergottite Martian meteorite (abstract #5008). *Meteoritics & Planetary Science* 45.

Stockstill-Cahill K. R., McCoy T. J., Nittler L. R., Weider S. Z., and Hauck S. A. II. 2012. Magnesium-rich crustal compositions on Mercury: Implications for magmatism from petrologic modeling. *Journal of Geophysical Research* 117:E00L15.

Stöffler D., Keil K., and Scott E. R. D. 1991. Shock metamorphism of ordinary chondrites. *Geochimica et Cosmochimica Acta* 55:3845–3867.

Takeda H., Mori H., Ikeda Y., Teruaki I., and Yanai K. 1984. Antarctic howardites and their primitive crust. *Memoirs of National Institute of Polar Research Special Issue* 31:81–101.

Tribaudino M., Mantovani L., Bersani D., and Lottici P. P. 2012. Raman spectroscopy of (Ca, Mg)MgSi2O6 clinopyroxenes. *American Mineralogist* 97:1339–1347.

Vaughan W. M. and Head J. W. 2014. Criteria for identifying mercurian meteorites (abstract #2013). 45th Lunar and Planetary Science Conference. CD-ROM.

Wang A., Jolliff B. L., Haskin L. A., Kuebler K., and Viskupic K. M. 2001. Characteriszation and comparison of structural and compositional features of planetary quadrilateral pyroxenes by Raman spectroscopy. *American Mineralogist* 86:790–806.

Wang Z., O'Neill H. S. C., Lazor P., and Saxena S. K. 2002. High pressure Raman spectroscopic study of spinel $MgCr_2O_4$. *Journal of Physics and Chemistry of Solids* 63:2057–2061.

Warren P. H., and Rubin A. E. 2010. Pyroxene-selective impact smelting in ureilites. *Geochimica et Cosmochimica Acta* 74:5109–5133.

Weber I., Bischoff A., and Weber D. 2003. TEM investigations on the monomict ureilites Jalanash and Hammadah al Hamra 064. *Meteoritics & Planetary Science* 38:145–156.

Weber I., Morlok A., Bischoff A., Hiesinger H., and Helbert J. 2014. Mineralogical and spectroscopic studies on NWA 7325 as an analogue sample for rocks from Mercury (abstract #1323). 45th Lunar and Planetary Science Conference. CD-ROM.

Weider S. Z., Nittler L. R., Starr R. D., McCoy T. J., Stockstill-Cahill K. R., Byrne P. K., Denevi B. W., Head J. W., and Solomon S. C. 2012. Chemical heterogeneity on Mercury's surface revealed by the MESSENGER X-ray Spectrometer. *Journal of Geophysical Research* 117: E00L05.

Weider S. Z., Nittler L. R., Starr R. D., McCoy T. J., and Solomin S. 2014. Variations on the abundance of iron on Mercury's surface from MESSENGER S-ray spectrometer observations. *Icarus* 235:170–186.

Weiss B, Downey B., Shuster D., Sharp T., Fu R., Kuan A., Suavet C., and Irving A. 2014. An unmagnetized early planetary body. AGU Fall Meeting, GP51B-3733.

White S. N. 2009. Laser Raman spectroscopy as a technique for identification of seafloor hydrothermal and cold seep minerals. *Chemical Geology* 259:240–252.

Yamaguchi A., Taylor G. J., Keil K., Floss Ch, Crozaz G., Nyquist L. E., Bogard D. D., Garrison D. H., Reese Y.

D., Wiesmann H., and Shih C.-Y. 2001. Post-crystallization rehaeating and partial melting of eucrite EET 90020 by impact into hot crust of asteroid 4 Vesta ~4.50 Ga ago. *Geochimica et Cosmochimica Acta* 65:3577–3599.

Yong W., Botis S., Shieh S. R., Shi W., and Withers A. C. 2012. Pressure-induced phase transition study of magnesiochromite ($MgCr_2O_4$) by Raman spectroscopy and X-ray diffraction. *Physics of the Earth and Planetary Interiors* 196–197:75–82.